inorganics

MDPI

Article

Copper(II) Complex with a 3,3′-Dicarboxy-2,2′-Dihydroxydiphenylmethane-Based Carboxylic Ligand: Synthesis, Spectroscopic, Optical, Density Functional Theory, Cytotoxic, and Molecular Docking Approaches for a Potential Anti-Colon Cancer Control

Ayman H. Ahmed [1,*], Ibrahim O. Althobaiti [2], Kamal A. Soliman [3], Yazeed M. Asiri [4], Ebtsam K. Alenezy [1], Saad Alrashdi [1] and Ehab S. Gad [1]

[1] Department of Chemistry, College of Science, Jouf University, Sakaka 72341, Aljouf, Saudi Arabia
[2] Department of Chemistry, College of Science, Islamic University, Medina 42351, Medina, Saudi Arabia
[3] Department of Chemistry, Faculty of Science, Benha University, P.O. Box 13518, Benha 345629, Qalyubia, Egypt
[4] Department of Chemistry, College of Science, Taif University, Taif 21944, Taif, Saudi Arabia
* Correspondence: ahfahmi@ju.edu.sa

Abstract: The chemical interaction of salicylic acid, formaldehyde, and sulfuric acid produced a disalicylic ligand (3,3′-dicarboxy-2,2′-dihydroxydiphenylmethane, DCM), which was then allowed to coordinate with copper (II) ions. The solid compounds' chemical structures were determined using elemental analysis, UV-Vis, FT-IR, MS, ^{1}H-NMR, PXRD, SEM, TEM, magnetic studies, as well as molecular modeling based on DFT (density functional theory) calculations. It was proposed that the ligand coordinates in a tetradentate fashion with the copper ion to give a square-planar binuclear complex. A significant difference in the diffraction patterns between Cu(II)–DCM (amorphous) and DCM (crystalline) was displayed using an X-ray diffraction analysis. Spherical granules were identified throughout through morphology analysis using SEM and TEM. UV-Vis spectra were used to quantify the optical characteristics such as the energy gap, optical conductivity, refractive index, and penetration depth. The band gap values that lie within the semiconductor region suggested that the compounds could be used for electronic applications. The optimized structure of the synthesized Cu(II)–DCM complex was investigated using DFT and TD-DFT (time-dependent density functional theory) at the B3LYP/6-31G(d, p) level, with the LANL2DZ basis set for Cu in an ethanol solvent and the gas environment modeled by CPCM. The experimental data suggest a square-planar geometry of the Cu(II) binuclear complex. The theoretical calculations support the proposed structure of the compound. The cytotoxicity of the DCM against HCT–116 (human colon cancer) cells was tested, and the outcome exhibited good inhibitions of growth. A molecular docking (MD) examination was carried out to illustrate the binding mode/affinity of the prepared compounds (DCM and Cu(II)–DCM) in the active site of the receptor protein [CDK2 enzyme, PDB ID: 6GUE]. The compounds formed hydrogen bonds with the amino acid residues of the protein, increasing the binding affinity from −7.2 to −9.3 kcal/mol through the coordination process. The information from this current study, particularly the copper complex, is beneficial for exploring new compounds that have anticancer potential.

Keywords: disalicylic ligand; copper complex; characterization; morphology; DFT; TD-DFT; biological assessment

check for updates

Academic Editors: Isabel Correia, Ana Maria da Costa Ferreira and Duncan H. Gregory

Received: 13 February 2025
Revised: 26 April 2025
Accepted: 30 April 2025
Published: 6 May 2025

Citation: Ahmed, A.H.; Althobaiti, I.O.; Soliman, K.A.; Asiri, Y.M.; Alenezy, E.K.; Alrashdi, S.; Gad, E.S. Copper(II) Complex with a 3,3′-Dicarboxy-2,2′-Dihydroxydiphenylmethane-Based Carboxylic Ligand: Synthesis, Spectroscopic, Optical, Density Functional Theory, Cytotoxic, and Molecular Docking Approaches for a Potential Anti-Colon Cancer Control. *Inorganics* **2025**, *13*, 151. https://doi.org/10.3390/inorganics13050151

Copyright: © 2025 by the authors. Licensee MDPI, Basel, Switzerland. This article is an open access article distributed under the terms and conditions of the Creative Commons Attribution (CC BY) license (https://creativecommons.org/licenses/by/4.0/).

1. Introduction

The investigated 3,3′-dicarboxy-2,2′-dihydroxydiphenylmethane (DCM) ligand (a synonymous name for 3,3′-methylendisalicylic acid) is regarded as an industrially important compound necessary for surface coatings and plastics [1]. Some applications in environmental chemistry, bioinorganic chemistry, metallic deactivators, electrochemistry, catalysis, and corrosion involve dicarboxy-dihydroxydiphenylmethane and its related transition metal complexes [2–6]. The two active groups (-OH and -COOH) in DCM make it crucial for coordination chemistry because they allow it to function as a polydentate ligand. When DCM couples with copper and iron ions, it readily yields chelated colorful compounds; additionally, Mg, Ba, Ni, and Zn-3,3′-dicarboxy-2,2′-dihydroxydiphenylmethane complexes have been prepared and described [5–7]. The following molecular formulae have been proven and reported: $[Ba(C_{15}H_{10}O_6)]\cdot 3H_2O$, $[Ba_2(C_{15}H_8O_6)]\cdot 8H_2O$, $[Mg(C_{15}H_{10}O_6)]\cdot 2H_2O$, $[Zn_2(C_{15}H_8O_6)(H_2O)_2(EtOH)_2]\cdot 2H_2O$, and $[Ni_2(C_{15}H_8O_6)(H_2O)_8]\cdot 7H_2O$ h. Although DCM is an old ligand, its coordination nature towards metal ions has not been adequately studied, and few efforts have been made. It is significant to recognize that 5,5′-methylenedisalicylic acid closely resembles the structure of DCM, and it can form solid complexes with rare-earth metals and aluminum [8,9]. The physicochemical study of square-planar Cu(II), Ni(II), and Co(II) chelates with the bis-oxime of 5,5′–methylene(salicylaldehyde) was explained by Patel et al. [10]. According to the findings, the complexes' thermal stability is arranged as follows: Ni(II) > Cu(II) > Co(II). On the other hand, information about the structure, characteristics, and pharmacological effects of extremely close 4,4′-methylenebis(3-hydroxynaphthalene-2-carboxylic acid and its transition metal complexes, such as copper(II) ions, has also been reported [11–14]. In terms of theoretical calculations, density functional theory (DFT) and time-dependent density functional theory (TD-DFT) have become essential tools in exploring the electronic and structural characteristics of metal complexes, providing detailed insights into molecular geometry, bonding interactions, and electronic transitions [15–20]. For transition metal complexes, these computational methods offer a powerful approach to understanding how metal–ligand interactions influence reactivity, stability, and photo-physical behavior, especially in different environments. In this study, DFT and TD-DFT calculations were applied to investigate the Cu(II)–DCM complex, aiming to elucidate its optimized geometry, electronic structure, and spectral properties. The structural parameters, including bond angles, bond lengths, and dihedral angles, were analyzed to confirm the stability and coordination environment of the complex. Additionally, TD-DFT calculations were employed to simulate electronic transitions, helping to match the theoretical results with experimental data. This combined approach enables a deeper understanding of the complex's reactivity and charge-transfer potential, with implications for its application in areas like catalysis and photochemistry. Every year, the rate of cancer incidence rises sharply; there are around 10.9 million new cases of cancer [21]. Colon cancer is one of the famous types among the majority of the population. It affects the colon or rectum and is called colorectal cancer (CRC). It is caused by abnormal colon cell proliferation and division. This aberrant cell division results in polyps, which can be either benign or malignant. The reason for these abnormal divisions is still not fully understood [22]. However, sedentary lifestyle, age and family history have all been linked to risk factors. People who are over 50 or consume alcohol, high amounts of tobacco (smoke), and high-fat diets are more likely to be diagnosed with colorectal cancer (CRC). By 2030, an analysis predicted that the number of new cases and deaths from CRC would increase globally by 60% to 2.2 million [23]. The disease can cause fatal harm and death. Common symptoms include low iron levels, constipation, diarrhea, blood in the stool, abdominal pain, and unexplained weight loss. Treatments include chemotherapy, radiation therapy, and surgery. Surgery is often employed if the tumor has

not transferred to other parts of the body. Chemotherapy involves undesirable side effects, although it may aid in tumor shrinking. Current treatments are not only costly but also often ineffective. It is therefore becoming more and more crucial to look for anti-colon cancer drugs in order to prevent the prevalence from rising quickly. The literature review indicated that several compounds, like curcumin [24], coumarin derivatives [25], ginger polysaccharide [26], and phenolic phytochemicals [27], have been studied as anti-colon cancer agents. Notably, salicylic acid possesses a structure analogous to that of DCM, which also showed an unquestionable anticancer effect [28,29]. Actually, research on DCM has not been conducted for human colorectal cancer yet, despite the fact that multiple compounds are known to protect against tumors in humans [28–30].

The molecular docking technique examines the binding capability of ligands to target binding sites in proteins (receptor or target molecules) [31,32]. The pharmacological management of colorectal cancer (CRC) involves several approaches, including the application of cytotoxic drugs like oxaliplatin and 5-fluorouracil. Compounds that block specific CRC targets are used in another pharmacological treatment approach. As the epidermal growth factor receptor (EGFR) and vascular endothelial growth factor (VEGF) are targets of CRC, drugs that block these targets, including cetuximab and ramucirumab, are used in the battle against CRC [33,34]. Since patients with colorectal cancer have been found to have overexpressed human cyclin-dependent kinase 2 (CDK2), inhibiting and/or down regulating this kinase has also been proposed as a treatment for CRC [35].

This work's objective was to reveal the molecular structure and optical and biological properties of a novel Cu(II)x3,3′-dicarboxy-2,2′-dihydroxydiphenylmethane complex in comparison to its corresponding ligand (DCM). Numerous fields, including chemistry, medicine, materials and crystal engineering, semiconductors, and electronic devices, could benefit from these properties. For this reason, DCM and its corresponding Cu(II) complex were studied by a combination of different techniques to identify the morphology, features, and structure of the synthesized materials. The band gap, skin depth (δ_p), optical conductivity, and refractive index were estimated as the optical characteristics. Furthermore, the Cu(II)–DCM complex was investigated using DFT and TD-DFT computations. This study also tried to find out the biological effects of the ligand on colorectal cancer. To show the binding affinity of the synthesized compounds with possible targets, molecular docking simulations of DCM/Cu(II)–DCM and the receptor proteins linked to the development of human colon cancer (HCT-116) were carried out.

2. Results and Discussion

The transitions in spectroscopy were interpreted and could serve to identify the molecule or give clues about the molecular structure. Various spectroscopic techniques were employed to describe and verify the solid structures.

2.1. Infrared Spectroscopy

When the FT-IR spectra of the copper complex and DCM ligand are compare, it can be concluded that DCM functions as a tetradentate, connecting to $2Cu^{2+}$ ions via the COOH and OH oxygen atoms while displacing a proton from each group. The following evidence supports this hypothesis: the negative shift of $\upsilon(C–O)_{phenolic}$ (DCM: 1281→Cu(II)–DCM: 1213 cm^{-1}). The disappearance of the phenolic OH and COOH groups in tandem with the formation of a υCOO^{-} at 1565 cm^{-1} for the complex suggested that the phenolic OH and COOH groups were involved in coordination with proton removal. The broad band that is obscured and attributed to the COOH intermolecular H–bond in the ligand (2390–2650 cm^{-1}) indicates that chelation caused the bond to break down. The υ_{asym}(C–O) vibration of the carboxylate group exists at 1565 cm^{-1}, whereas

at 1361 cm^{-1} υ_{sym}(C–O) occurs. The separation value of 204 cm^{-1} between the υ_{asym} and υ_{sym} bands indicates that the carboxylate group binds to the Cu(II) ion in a monodentate manner [36]. Two weak bands centered at 582 and 604 are most probably due to the copper–oxygen bond ($Cu–O_{phenolate}$/$Cu–O_{carboxylate}$) [37,38]. Stretching vibrations at a frequency of ≈3550 cm^{-1} (υOH_{water}) and two considerably weaker bands corresponding to rocking (OH_{water}: 860 cm^{-1}) and wagging (OH_{water}: 620 cm^{-1}) frequencies are suggested due to coordinated water in the copper complex.

2.2. Ultraviolet–Visible Spectroscopy and Magnetic Investigation

The Cu(II) complex that displayed a distinct broad band at ~700 nm originates from the combination of the $d_{xy}\rightarrow d_{x^2-y^2}$, d_{yz}, $d_{xz}\rightarrow d_{x^2-y^2}$, and $d_{z^2}\rightarrow d_{x^2-y^2}$ transitions in a distorted square-planar shape [39]. A second band was detected at 560 nm, primarily caused by a ligand–metal charge transfer (LMCT). The existence of two new remarkable transitions in the complex spectrum at 700 and 560 nm in comparison to the free ligand (Figure 1) indicated the formation of the desired copper complex [36]. A suggestion for the square-planar geometry of the complex is proposed based on the following: (1) Since 3d has nine electrons and 4s is vacant in Cu(II), if the ligand has a strong field, the one unpaired electron will be moved to 4p, allowing Cu to form the most stable inner orbital complex (dsp^2 hybridization), which is equivalent to a square-planar geometry. (2) Cu(II), with a d^9 configuration, can form square-planar or octahedral geometry. The fifth and sixth bonds are typically lengthened by the notable Jahn–Teller distortion of the octahedral coordination. Since the separated complex is a brown solid whereas the majority of distorted octahedral Cu(II) complexes are green or blue, the complex's octahedral structure is not considered here.

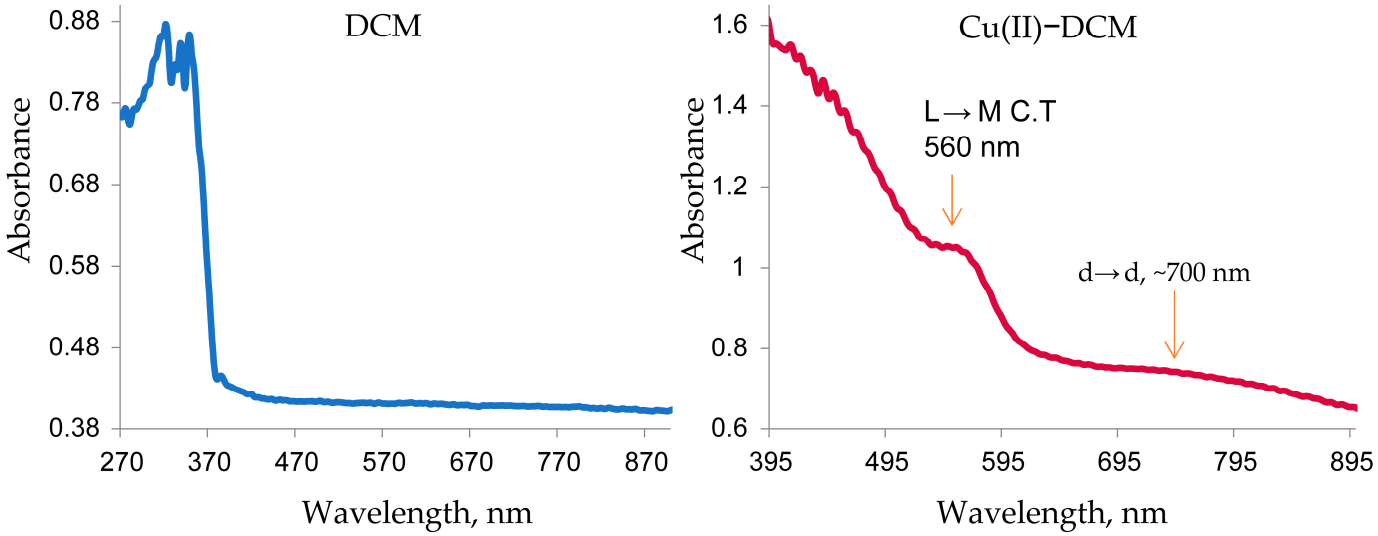
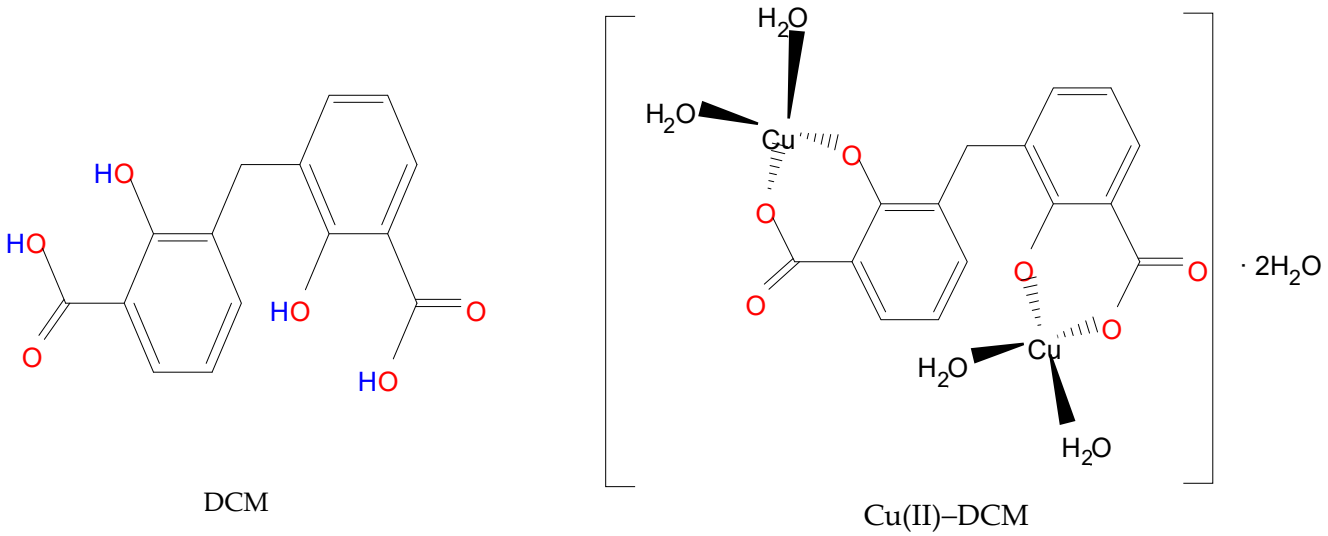


Figure 1. Electronic spectra of DCM and Cu(II)–DCM.

For first-row transition metals, the orbital angular momentum is often removed or partially quenched by the interaction of the ligands with the partially occupied d orbitals, and the magnetic moment corresponds to the 'spin only' formula. Regarding magnetic analysis, the experimental magnetic moment of the synthesized binuclear Cu(II) complex (μ_{eff} = 2.49 BM) is greater than that of the computed spin-only value (μ_s = 1.73 BM). This result is most probably due to the presence of two closed Cu(II) ions in the molecular structure of the complex (Scheme 1), which leads to a Cu–Cu interaction (Cu↑…↑Cu) and magnetic reinforcement [40]. Actually, the resulting high magnetic moment of the Cu(II) complex emphasizes that the unpaired electron spin of two Cu(II) ions is in the

same direction. The following is an explanation of this claim: (1) The DCM ligand is more flexible due to the presence of two phenyl rings joined by a twisted -CH_2- moiety. Because of this, the two phenyl rings have ample freedom to twist around the -CH_2- [41], resulting in close proximity for the two Cu(II) centers. (2) Small water molecules that are planarity-coordinated do not obstruct the copper centers' approach. As a result, the proposed square-planar geometry can be supported by the μ_{eff} value = 2.49 B.M. for the binuclear copper complex, which is in reasonable agreement with the computed spin-only magnetic moment.



Scheme 1. Structure of DCM in comparison to Cu(II)–DCM complex.

In light of the foregoing conclusions, the DCM and Cu(II)–DCM complex can be displayed by Scheme 1. In fact, the complex monomer structure was suggested despite its total insolubility on the basis as follows: (1) The ligand's solubility was hindered by the polar groups (2COOH and 2phenolic-OH) disappearing due to coordination with the Cu^{II} ions. Also, the large molecular size of the complex (it contains two phenyl rings) reduces its solubility. It is more difficult for solvent molecules to wrap around larger molecules in order to dissolve them. (2) The SEM analysis indicates the existence of complex particles in the non-nano-scale that might be an indicator of their big size, which reduces the surface area exposed to the solvent and, consequently, their low solubility. (3) The consistency of the theoretical and experimental data was observed. (4) The formulation of monomeric structures with extremely near ligands was emphasized in several references. Methylenedisalicylate has been used to separate the monomer forms of Ba^{II}, Mg^{II}, Zn^{II}-, and rare earths [7,8]. The complexes of methyl salicylate (MS) with La^{III}, Gd^{III}, Tb^{III}, and Lu^{III} have the formula $Ln(MS)_3$ and were demonstrated by Tobita et al. [9]. Two types of monomeric methyl salicylate Cr(III) complexes, which are $[Cr(SA)_2(en)]TBA{\cdot}H_2O$ and $[Cr(SA)(en)_2]Br{\cdot}H_2O$ (TBA = Tetrabutylammonium, SA = salicylate, en = ethylenediamine), have been produced and verified by X-ray crystallography [42]. Furthermore, for disalicylic acid ligands with different spacers between two salicylic acid unions, the selective extraction of Pb(II) over Cu(II) as well as Cd(II), Ni(II), and Zn(II) was investigated. Pb(II) complexes have stoichiometries of 2:1 and 1:1 ligand–metal ions, whereas Cu(II) ions have a 1:1 stoichiometry [43].

2.3. Powder XRD Studies

The Cu(II)–DCM complex and DCM ligand were documented by X-ray diffraction patterns. Table 1 displays the diffraction data, which includes the crystallite size and

inter-planar distances d (Å). Figure 2 demonstrates that DCM is crystalline, meaning that the molecules are arranged in a unique geometric structure. The good crystallinity is demonstrated by the apparent sharp peaks in the XRD patterns of the DCM particles [44]. The XRD pattern of Cu(II)–DCM in Figure 2 suggests an amorphous character, demonstrating the random arrangement of the component particles. Due to the absence of regular, symmetric crystal planes, the copper complex does not exhibit distinctive, sharp diffraction patterns. The diffraction patterns of the copper complex show a considerable difference from the free ligand, supporting a successful chelation process. Since the amorphous Cu(II)–DCM solid lacks an ordered atomic structure, its melting point is not clearly defined. The amorphous complex will therefore have unique and useful features that give it the ability to be sculpted into useful shapes when heated (as used in the manufacture of bendable and flexible electronics), due to the absence of a well-defined melting point. Indeed, the unique characteristics of amorphous solids have led to technological advancements in materials science and drug development. Thus, the special properties of amorphous Cu(II)-DCM can be used to create resistant coatings and manufacture drugs with improved bioavailability (the degree to which the active component (drug) reaches the site of action via entering the systemic circulation). According to the Scherrer equation [45], $D = 0.89\lambda/\beta \cos\theta$, where λ is the X-ray wavelength (1.54 Å for CuKα radiation), θ is the peak location, and β is the full width at half maximum; it was discovered that the crystallite size of the DCM is 14 (Table 1), but the equation could not be applied to Cu(II)-DCM due to its amorphous form.

Table 1. DCM and Cu(II)–DCM complex XRD data.

Compound	XRD Data			
	Angle (*d*-Value)	θ°	β (rad)	D (nm)
DCM	13.21° (6.699 Å), 15.32° (5.778 Å), 16.24°(5.454 Å), 19.17° (4.626 Å), 19.80° (4.481 Å), 22.70° (3.915 Å), 23.42° (3.795 Å), 26.52° (3.358 Å), 29.79° (2.997 Å), 30.99° (2.883 Å), 34.08° (2.629 Å), 35.86° (2.502 Å), 38.49° (2.337 Å), 40.30° (2.236 Å), 42.07° (2.146 Å)	23.47	0.011	14.40
Cu(II)–DCM	7.32° (12.068 Å)	-	-	-

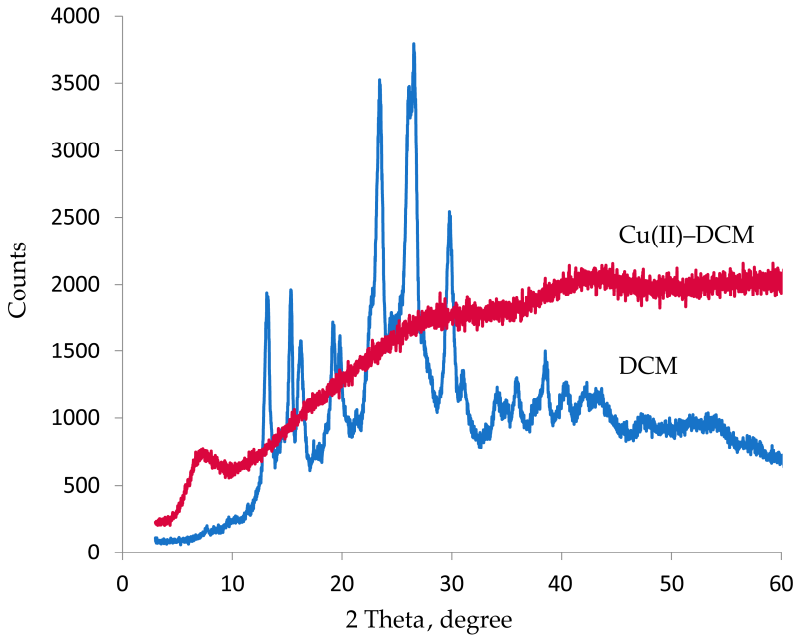


Figure 2. XRD graph of DCM and Cu(II)–DCM.

2.4. Optical Characteristics

Figure 3 displays the differences in optical properties between the ligand and copper complex. The indirect band gap energy of the produced materials due to the electron–photon–phonon interaction was measured since it affects the ability of the materials to absorb light. The energy gap of the DCM (3.20 eV) and Cu(II)–DCM (1.85 eV) compounds were found to be in the range of semiconductors, as seen in Figure 3a. According to the results, the ligand conductivity is similar to that of ZnO, E_g = 3.37, as well as GaN, E_g = 3.4, whereas Cu(II)–DCM conduction is similar to that of Se, E_g = 1.74; CdSe, E_g = 1.73; GaAs, E_g =1.41; CdTe, E_g = 1.43; and CuO, E_g =1.2 [46,47]. An electron in the conduction band cannot fall straight to the valence band; instead, it must undergo a change in momentum and energy, with a portion of that energy typically being released as heat to the lattice instead of as an emitted photon. This is recognized as the materials' acquired indirect band gap. This will of course determine the appropriate application on the selected materials. As a worthy mention, the indirect transition can occur due to some defects in the lattice structure of the materials. The reason for a larger E_g value of DCM compared to its Cu(II) complex comes from the tendency of the copper ion to increase the width of its levels by accepting the electrons of a ligand into its vacant outer shell throughout the chelation process. This, in turn, reduces the band gap. Because a smaller band gap allows for easier electronic transitions between the HOMO and LUMO energy states, this suggests that the electric conductivity of the Cu(II)–DCM complex will be higher than that of free DCM [48]. Applications in electronics may use the synthesized compounds (DCM and Cu(II)–DCM), whose band gap values are in the semiconductor range [49].

Determining the ligand and complex refractive indices is crucial. Optic devices, such as modulators, switches, and filters, require an understanding of optical refractive indices. Furthermore, the refractive index is an important physical property that is frequently used in chemistry to evaluate purity. The following relationship can be used to express the refractive index values (n) of the compounds [50,51]: $n = \frac{1+\sqrt{R}}{1-\sqrt{R}}$, where R is the predicted normal reflectance determined by applying the formula R (reflectance) + T (transmittance) + A (absorption) = 1. Based on the UV-Vis data (electronic spectra), the ligand and complex's R values are determined as follows: R(reflectance) of the DCM ligand = $1 - T$ (transmittance, DCM) $- A$ (absorption, DCM); R(reflectance) of Cu(II)-DCM = $1 - T$ (transmittance, Cu(II)-DCM) $- A$ (absorption, Cu(II)-DCM). The changes in the refractive index (n) in relation to the wavelength (λ, nm) are shown in Figure 3b. It is observed that the refractive index varies with the wavelength of the incident light beam due to specific interactions between photons and electrons [52]. The drawing also illustrates the impact of complexation on the refractive index of the free ligand where chelation causes a variation in its n values. With the exception of 270–301 and 330–340 nm, the data in Figure 3c clearly show that the refractive index of the DCM ligand is higher than that of the associated copper complex. The values of n and the wavelength of the incident light are used to determine the optical conductivity (σ_{opt}), which is expressed as $\sigma_{opt} = nck/\lambda$ [53]. Here, n, c, k, and λ are the refractive index as mentioned above, the velocity of the light (3×10^8 m/s), the extinction coefficient ($\alpha\lambda/4\pi$), α = 2.302A (absorbance) and π = 3.14, and the wavelength, respectively. The σ_{opt} values for the two compounds change and rise with increasing photon energies, as Figure 3c plainly shows. Obviously, Cu(II)–DCM has a higher optical conductivity more commonly than DCM.

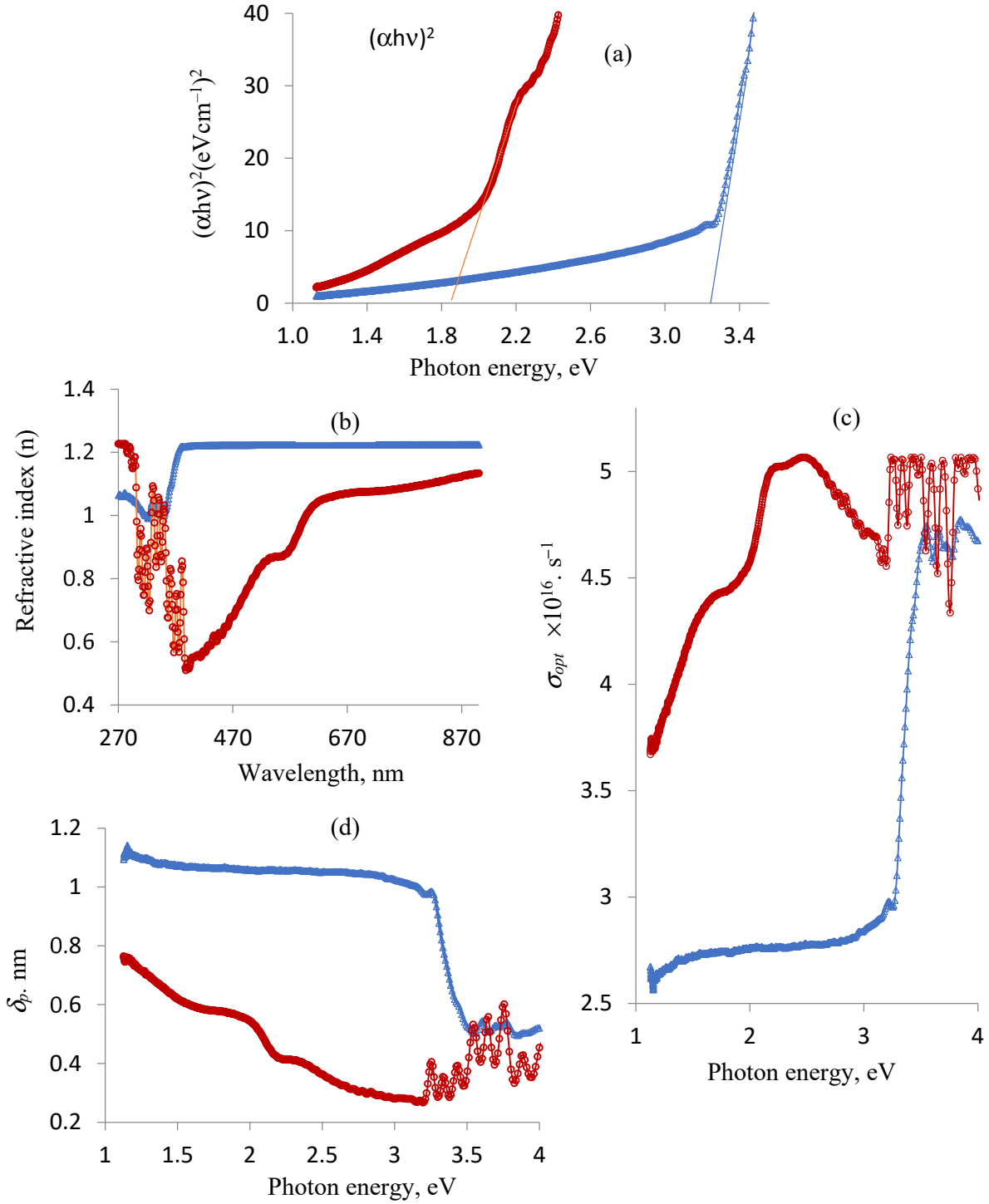


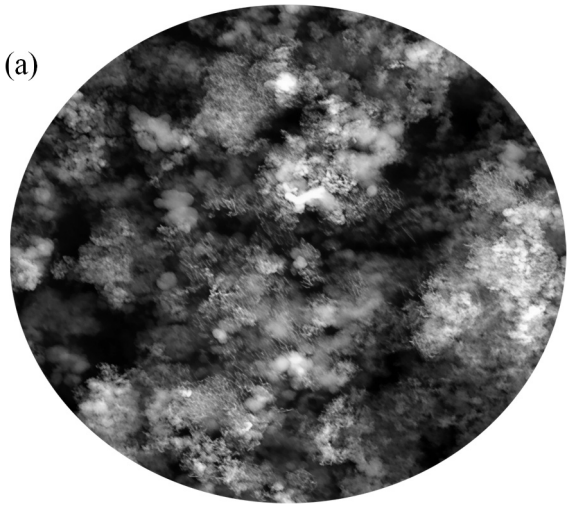
Figure 3. Ligand and complex changes in optical properties: (**a**) band gap energy, E_g; (**b**) refractive index, n; (**c**) optical conductivity, $\sigma_{opt;}$ and (**d**) penetration depth, δ_p. Note: DCM (blue line) and Cu(II)-DCM (maroon line).

The penetration depth through the substances (skin depth) is reached when the incident radiation intensity, passing through the material, drops to roughly 37% of its initial value. It can be calculated using the formula $\delta_p = \lambda/4\pi k$, where k and λ stand for the extinction coefficient calculated before and the wavelength assigned from the ligand/complex spectrum, respectively. Depending on the characteristics of the substance and the radiation's wavelength, electromagnetic radiation may either instantly vanish or permeate it very deeply. δ_p as a function in the $h\nu$ fluctuation for the compounds

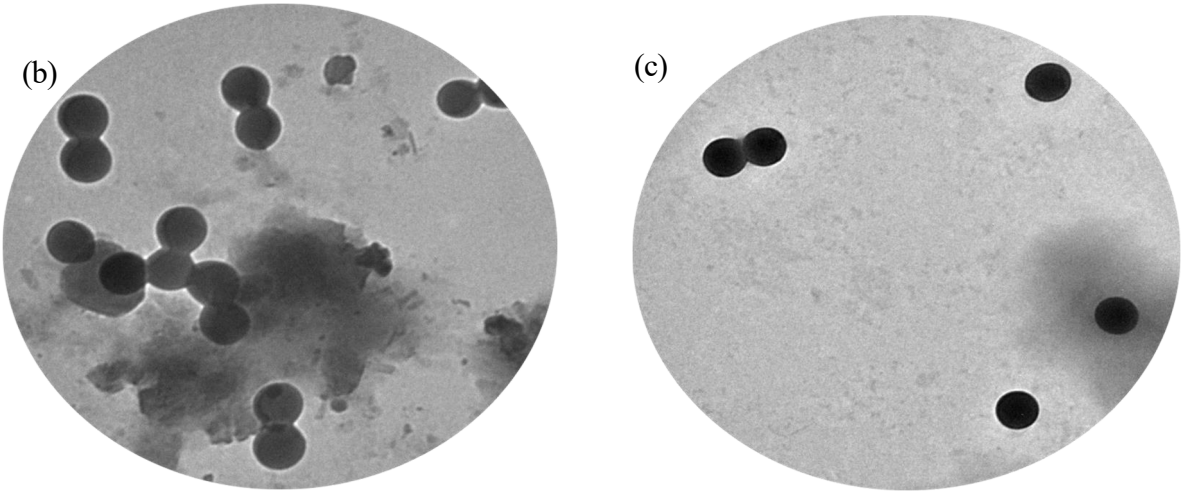
is displayed in Figure 3d. Notably, the free DCM ligand is more penetrated than its corresponding copper complex up to photon energy 3.5 eV, after which the behavior becomes irregular.

2.5. Morphology (SEM and TEM)

Figure 4a shows the resulting SEM micrograph of the copper complex. The compound exhibited spherical granules. At the same magnification (26,100×), the transmission electron microscopy (TEM) analysis of DCM and Cu(II)–DCM was also carried out to confirm the morphological characteristics (Figure 4b,c). Clearly, both the complex micrographs and the ligand exhibited regular, spherical forms [54,55] as obtained by SEM analysis. The Cu(II)–DCM and DCM average particle sizes, according to the TEM images, are 163 and 156 nm, respectively. Evidently, the TEM and the SEM results agree well in determining the form of the particles for the copper complex. In spite of the fact that the compounds are not within the nano-range, they can contribute to drug development.



HV: 20.00 kv; HFW: 41.4 µm; Mag: 10,000 ×; Det: LFD; WD: 11.8 mm; Spot: 3.5.



Print Mag: 26100 × @51 mm; Direct Mag: 6000 ×; HV: 80.0 kv; AMT Camera System.

Figure 4. Morphological pictures of Cu(II)–DCM and DCM: (**a**) SEM of Cu(II)–DCM, (**b**) TEM of DCM; (**c**) TEM of Cu(II)–DCM.

As will be discussed later, it is possible to use the investigated compounds to manufacture anti-colon cancer drugs with improved bioavailability.

2.6. Theoretical Study

The Chem. Draw Professional 16 program was used to identify the MM2 (molecular mechanics) and MMFF94 (molecular mechanics force field) energies, HOMO and LUMO forms, and optimal lowest energy structure for the compounds (Figure 5). The results of the MM2 and MMFF94 minimizations were as follows: (1) DCM, MM2 minimization: Stretch: 1.9692; Bend: 7.6113; Stretch–Bend: −0.1191; Torsion: −16.5000; Dipole/Dipole: 3.8687; Total Energy: 1.7 kcal/mol; MMFF94 minimization: Final Energy: 32.2 kcal/mol. (2) Cu-DCM, MM2: Stretch: 51.5546; Bend: 156.3496; Stretch–Bend: 0.2594; Torsion: −7.7225; Dipole/Dipole: 10.1365; Total Energy: 209.4 kcal/mol; MMFF94 minimization: Final Energy: 73.2 kcal/mol.

A computational approach was performed to confirm the experimental results of the copper complex. The optimized geometry of the synthesized complex Cu(II)–DCM was calculated at the B3LYP/6-31G(d, p) level of theory, with an effective core potential (LANL2DZ) [56] for the copper atom in ethanol depicted in Figure 6. Table 2 represents the calculated structural parameters, including dihedral angles, bond angles, and bond lengths. The carbon–carbon bonds within the ligand range from 1.39 to 1.43 Å, which are typical for C–C bonds in aromatic systems, suggesting stable conjugated π-bonding. The values of bond distances (1.87(O25-Cu30), 1.88(Cu30-O27), 2.03(Cu30-O31), and 2.06(Cu30-O34) as well as angels (96.3(O25-Cu30-O27), 88.8(O25-Cu30-O31), 90.0(O31-Cu30-O34), and 85.0(O34-Cu30-O27) around the copper center (Table 2) affirmed a distorted square-planar structure for the copper complex. A slight change in bond lengths points to the distortion while the angle values near 90° imply a square-planar geometry. (The bond angles of the ideal square-planar structure are 90 degrees.) This theoretical conclusion is in good agreement with the experimental results. On the other hand, the Cu–O bonds with O25 and O27 have distances of 1.87 Å and 1.88 Å, respectively, indicating stable coordination. These distances align well with typical Cu–O coordination bonds, showing that the copper is well coordinated within the ligand framework. The angles around the Cu center, such as O25-Cu30-O27 at 96.3°, slightly deviate from the ideal square-planar geometry, indicating a slight distortion likely due to steric or electronic influences from the surrounding ligands. The dihedral angles, such as 57.5° (C2-C3-C9-C12), indicate non-planarity in parts of the complex, which could affect the orbital overlap and potentially influence the electronic properties. As seen in Figure 6, the LUMO form is likely located around the copper and coordinated oxygen atoms, whereas the HOMO form shows significant contributions around the ligand framework. This distribution suggests that the electron density is shared between the metal center and ligand, enabling potential charge-transfer interactions.

Figure 7 shows the NBO (Natural Bond Orbital) charges and electrostatic potential (ESP) for the complex Cu(II)–DCM. NBO analysis helps in understanding donor–acceptor interactions and the nature of bonding within the complex. For Cu(II), the analysis would likely show back-donation interactions from the ligands to the metal center, reinforcing bond stability. Back-donation helps distribute electron density more evenly across the complex. This redistribution stabilizes the system, especially when the metal center has a high positive charge, as with Cu(II). By sharing some of the electron density from the ligands, the metal center's effective positive charge is reduced, which stabilizes the complex. The ESP map reveals regions of electron density, with blue areas representing regions of lower electron density (positive potential) around the metal center and red indicating higher electron density around the oxygen atoms. This charge distribution aligns with the

anticipated polarity and is essential for understanding intermolecular interactions with surrounding environments.

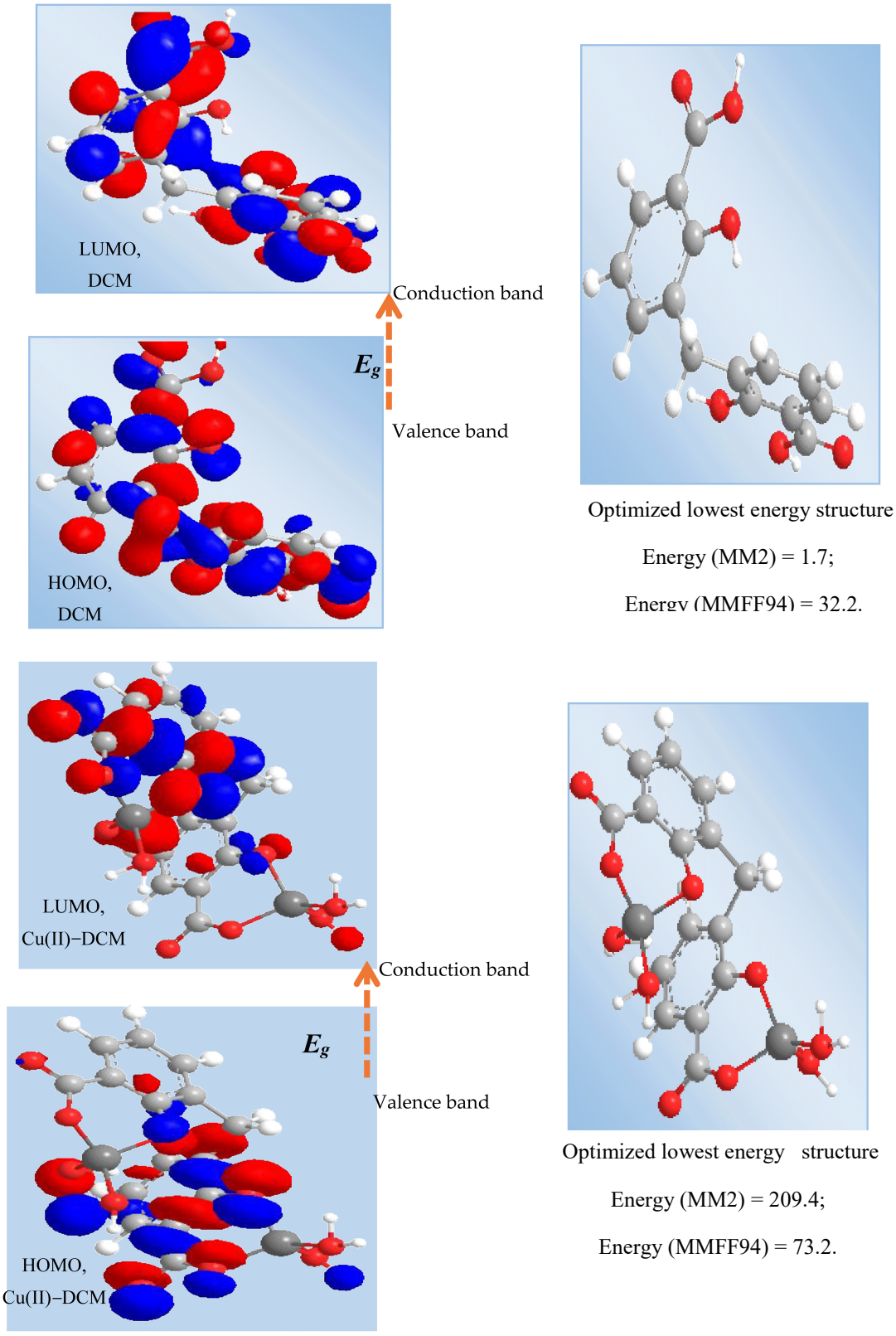


Figure 5. HOMO and LUMO transition of ligand and Cu(II) complex. Note: HOMO = Highest Occupied Molecular Orbital; LUMO = Lowest Unoccupied Molecular Orbital; MM2 = molecular mechanics; and MMFF94 = molecular mechanics force field.

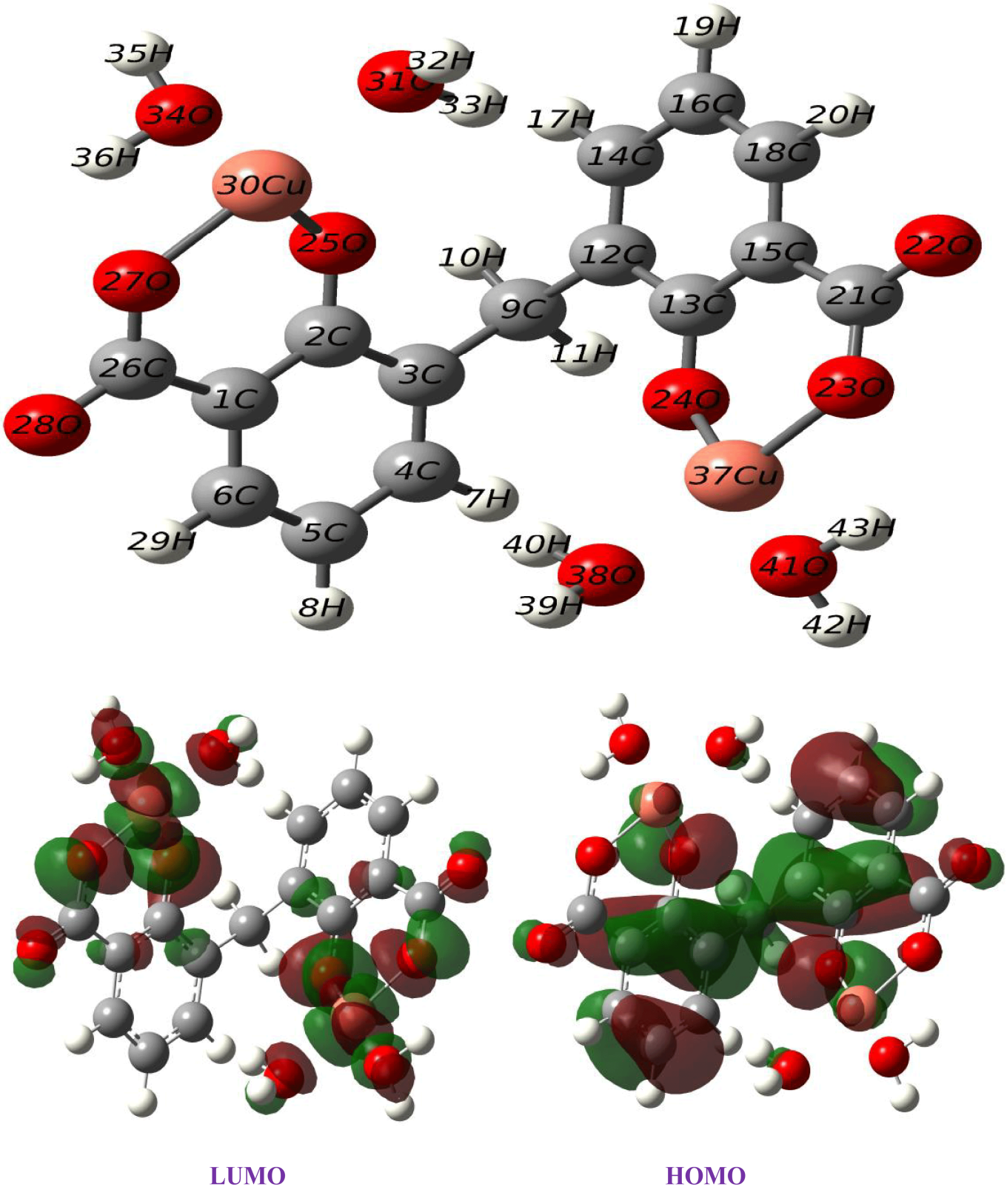
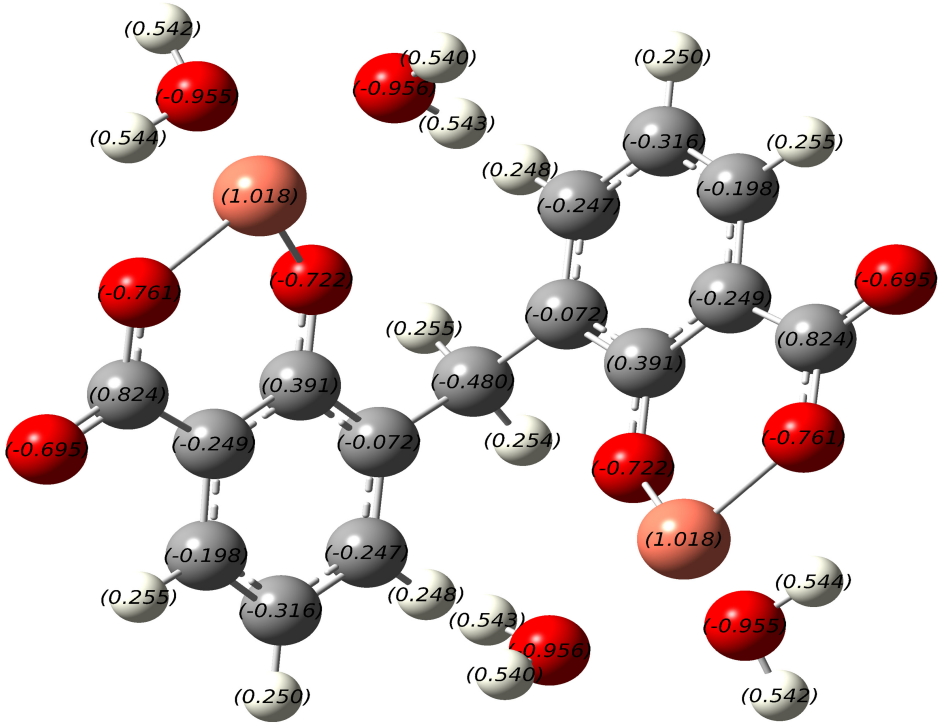


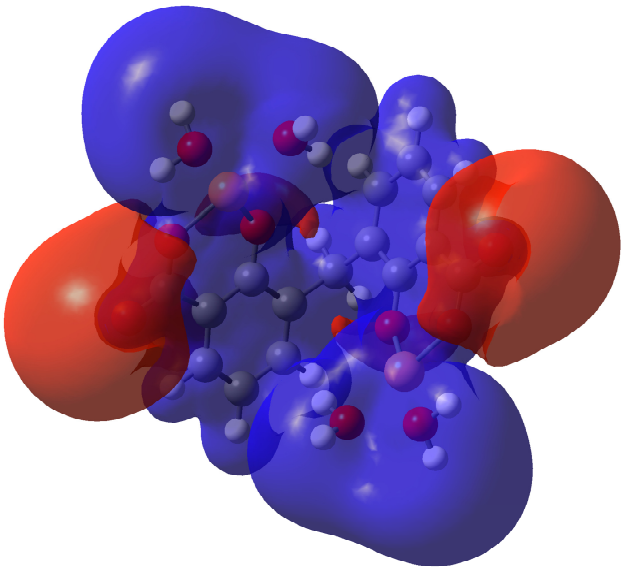
Figure 6. Optimized structure and frontier orbitals of Cu(II)–DCM complex.

Table 2. Optimized geometrical parameter of the Cu(II)–DCM complex calculated at the B3LYP/6–31g (d, p) level of theory. The effective core potential was employed using the LANL2DZ (Cu) basis set.

Optimized Geometrical Parameter	Cu(II)–DCM
Bond distance, Å	1.43 (C1-C2)(C2-C3), 1.39(C3-C4)(C5-C6), 1.40(C4-C5)(C6-C1), 1.32 (C2-O25), 1.87(O25-Cu30), 1.88(Cu30-O27), 2.03(Cu30-O31), 2.06(Cu30-O34), 1.31(O27-C26), 1.24(C26-O28), 1.51(C3-C9).
Angle (°)	119.0(C1-C2-C3), 121.7(C3-C4-C5), 124.3(C1-C2-O25), 96.3(O25-Cu30-O27), 88.8(O25-Cu30-O31), 90.0(O31-Cu30-O34), 85.0(O34-Cu30-O27), 119.7(O27-C26-C1).
Dihedral angle (°)	57.5(C2-C3-C9-C12), −2.09(C1-C26-O27-Cu30), 2.09(C9-C3-C2-O25)



NBO



ESP

Figure 7. Charges obtained from NBO and electrostatic potential map (ESP) of Cu(II)–DCM complex.

The HOMO and LUMO (frontier molecular orbitals, FMOs) characteristics and their energy gap are essential in quantum chemistry calculations, providing insights into a molecule's chemical reactivity and kinetic stability [57,58]. Generally, a wider energy gap correlates with higher stability and hardness, whereas a narrower energy gap indicates greater reactivity, polarizability, and softness. This decrease in the energy gap also facilitates a more substantial electronic charge transfer from the ligand to the metal ion [59]. Theoretical calculations for the quantum chemical parameters of the complexes are seen in Figure 8 [56]. Experimentally, the DCM ligand has an energy gap of 3.2 eV, which is significantly higher than that of the Cu(II)–DCM complex. This large gap indicates that the ligand has a relatively stable electronic structure, with limited reactivity under typical conditions. Upon complexation with Cu(II), the energy gap decreases to 2.19 eV, which suggests a stronger electronic interaction between Cu and the DCM ligand. This reduction implies that the complex is more reactive and has increased potential for electron-transfer processes. The calculated gap in the gas phase (2.05 eV) is very close to the experimentally observed value (1.85 eV), showing good agreement and supporting the reliability of the computational method. The decrease from 3.2 eV to 2.05 eV by complexation indicates significant orbital mixing between Cu and the DCM ligand, facilitating electronic transitions at lower energies. In ethanol, the energy gap increases slightly to 2.30 eV. This shift may be due to solvent stabilization effects, where the polar ethanol solvent stabilizes the complex's electronic states differently than in the gas phase, slightly increasing the HOMO-LUMO gap. The HOMO-LUMO values in different phases imply that the complex reactivity and stability could be tuned by the environment, with polar solvents slightly stabilizing the complex.

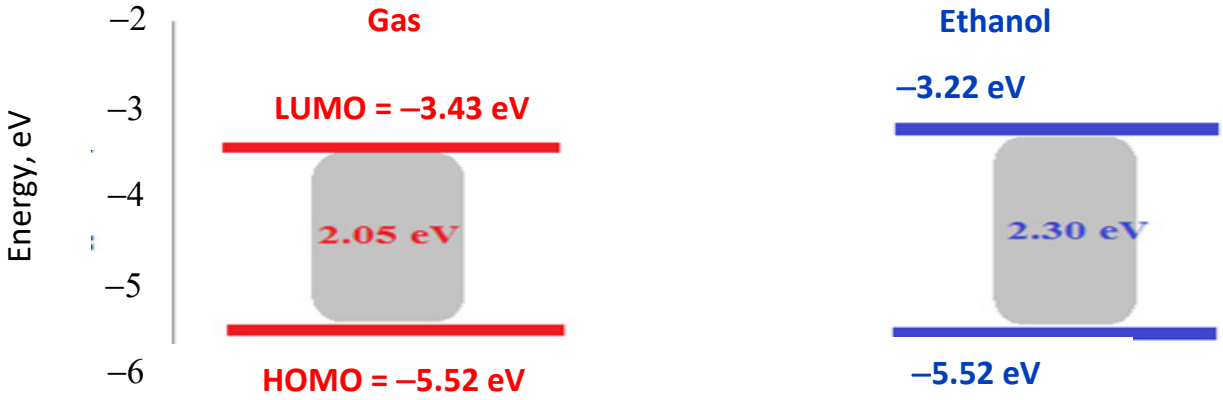


Figure 8. HOMO, LUMO, and energy gap values of Cu(II)–DCM complex in gas and ethanol phase.

TD-DFT calculations were conducted on the optimized structures of the Cu(II)–DCM complex to determine their spectral transitions and electronic structure. Using CPCM, these TD-DFT computations were carried out in EtOH. The experimental absorption maximum (λ_{max}) of the Cu(II)–DCM complex is observed at 566 nm. TD-DFT calculations provide several transitions near this wavelength, with notable peaks at 562.0 nm and 561.6 nm as summarized in Table 3. These calculated wavelengths align closely with the experimental value, validating the TD-DFT method's effectiveness in predicting the complex's electronic transitions. The transition at 562.0 nm mainly involves orbitals HOMO-11 to LUMO+1 (17%) and HOMO-10 to LUMO (18%), indicating that the transition primarily involves the electron density from lower occupied orbitals (H-11 and H-10) to unoccupied molecular orbitals near the LUMO level. This suggests a degree of delocalization in the excitation process, likely influenced by the metal–ligand charge transfer. The transition at 561.6 nm is driven by contributions from HOMO-11 to the LUMO (18%) and HOMO-10 to LUMO+1 (16%). These transitions, which involve both metal-centered and ligand-centered orbitals,

demonstrate that the Cu(II)–DCM complex experiences mixed metal-to-ligand charge-transfer (M→L CT) and ligand-to-metal charge-transfer (L→M CT) characteristics. The close alignment of the calculated λ_{max} with the experimental value further suggests that these transitions accurately capture the complex electronic environment in a polar solvent. The primary transitions around 561–562 nm involve complex orbital interactions that enhance the compound's charge-transfer characteristics, making this complex responsive to visible light, with potential applications in photoactive materials or catalysis. The oscillator strength at absorption 685.4 nm (experimentally at 700 nm) is the highest among those studied, indicating strong absorption at this wavelength. Oscillator strength measures the intensity of an electronic transition, and a high value suggests that this transition is highly possible and efficient. The H-1(B)→LUMO(B) component being dominant highlights that this excitation involves significant interaction between the occupied orbitals just below the HOMO and the unoccupied orbitals of the LUMO, suggesting overlapping transitions that involve both metal and ligand orbitals. This M-L overlapping indicates a successful complexation process.

Table 3. UV data of Cu(II)–DCM complex.

No.	Energy (eV)	Wavelength (nm)	Osc. Strength	Major Contribs.
1	1.16	1064.1	0.0013	H-1(B)→L + 1(B)(28%), HOMO(B)→LUMO(B)(62%).
2	1.18	1050.7	0.0032	H-1(B)→LUMO(B)(35%), HOMO(B)→L + 1(B)(55%).
3	1.81	685.4	0.0122	H-1(B)→LUMO(B)(61%), HOMO(B)→L + 1(B) (38%).
4	1.82	679.5	0.0021	H-1(B)→L + 1(B)(67%), HOMO(B)→LUMO(B) (32%)
7	2.20	562.0	0.0084	H-11(B)→L + 1(B) (17%), H-10(B)→LUMO(B) (18%).
8	2.21	561.6	0.0089	H-11(B)→LUMO(B) (18%), H-10(B)→L + 1(B) (16%).

2.7. Cytotoxic Assay

In fact, Cu(II)-DCM could not be investigated in vitro because of the complex's insoluble nature in solvents, which limits the evaluation of its cytotoxic potential. However, the DCM ligand was evaluated in test conditions against human colon (HCT–116) cancer cells and the cell survival data are shown in Figure 9. It was shown that 167.9 ± 11.4 µM is the ligand concentration that inhibits half of cell proliferation (IC_{50}). The inhibition of DCM may really be caused by a number of reasons, such as the following: (1) the DCM ligand's reaction with the metal ions in the cell fluid could affect or even stop the activity of the cells; (2) within the active site, ligand–protein interactions include covalence, Van der Waals, hydrophobia (staking), and H-bonding; and (3) DCM and transition metals found in cancer cell metallo-enzymes produce chelates that prevent multiple critical enzymatic processes, ultimately leading to the death of the cancerous cells [60]. Since the structure of DCM closely mimics that of a naturally occurring, non-toxic, and anticancer salicylic acid, DCM's impact can be regarded as an expected result. It is important to note that salicylic acid is a common safe ingredient in food and cosmetic formulations as well as pharmaceutical products [61,62].

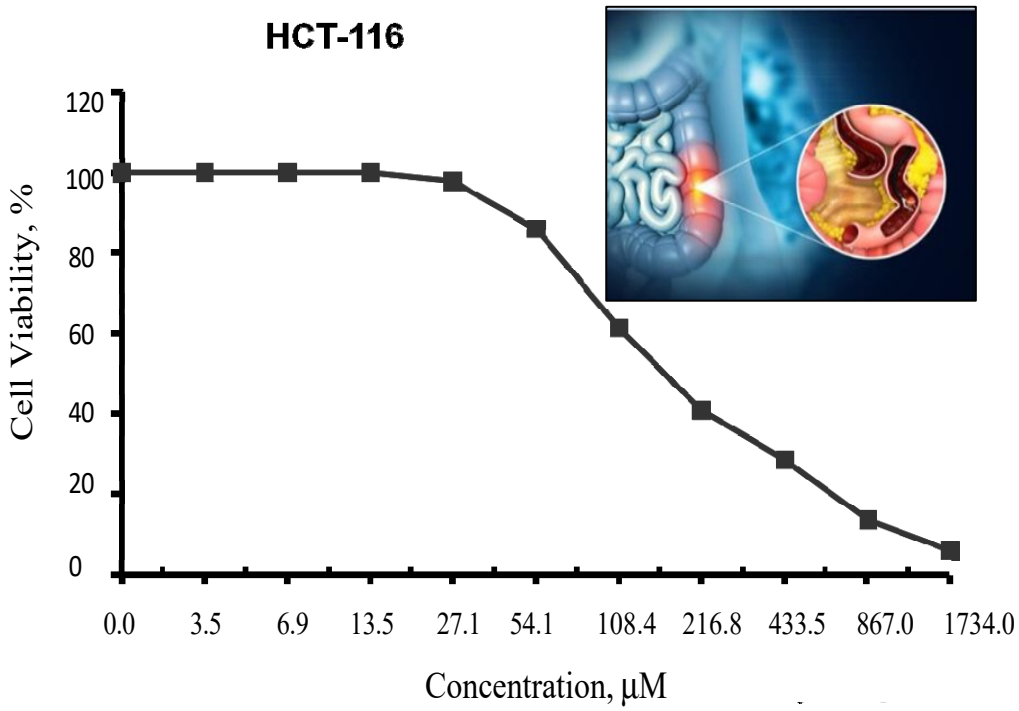


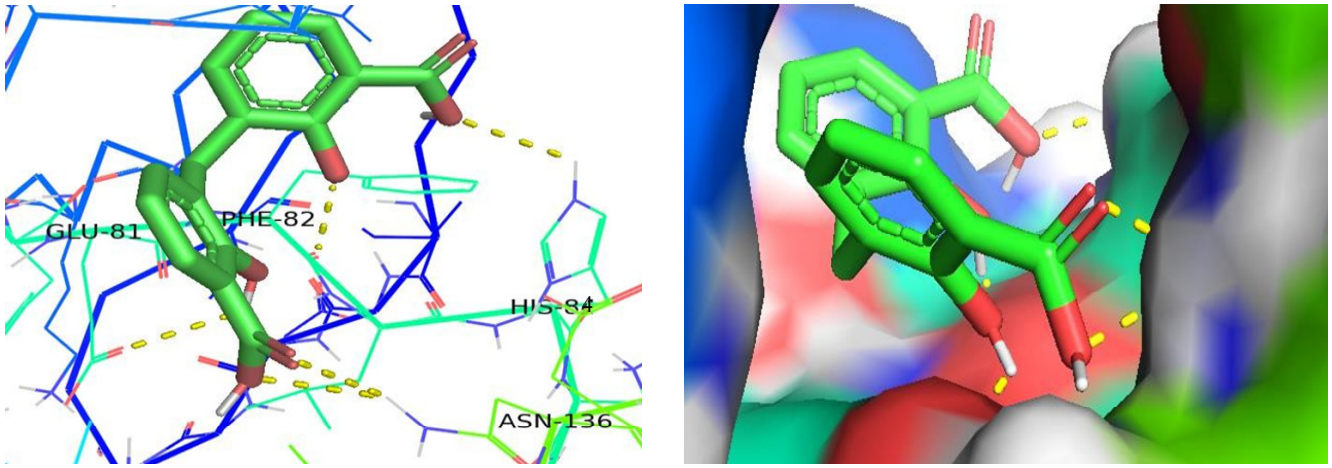
Figure 9. Inhibitory action of the DCM ligand against colon carcinoma cells (HCT–116). The graphic in Figure 9 depicts the development of colon cancer, including the formation of polyps. Polyps are small clusters of cells or masses that may seem like small bumps on the colon's interior lining.

2.8. Molecular Docking Simulation

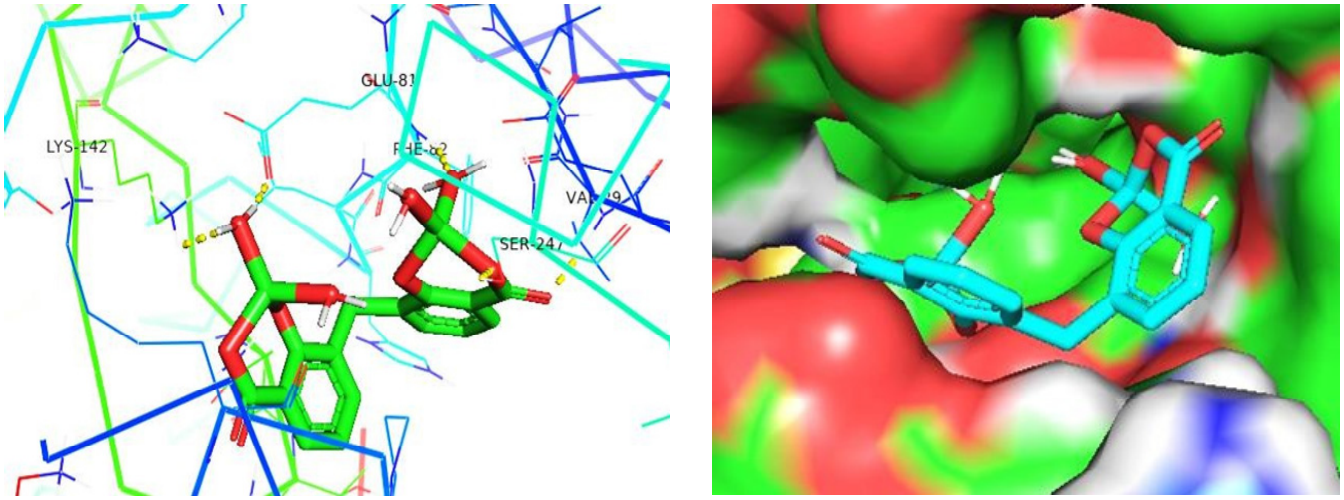
In the current work, the interaction between the separated compounds and the target (protein/enzyme) was examined using molecular docking [56]. The main bonding interactions between the compounds and the protein's amino acid residues were displayed, along with the binding affinity, which characterizes the strength of binding with the receptor. PyRx, a virtual screening tool, was used to dock compound–target protein interactions, and PyMol was used to visualize the results. The findings of the molecular docking study for the researched receptors are displayed in Table 4 and Figure 10. The compounds and proteins are generally thought to have good docking action if the docking score is greater than five; high docking activity is thought to exist if the docking result is greater than seven [63]. With a binding affinity of −7.2 kcal/mol, DCM creates the main H-bond interactions [56] with the amino acids Phe-82, Glu-81, His-84, and Asn-136 of the 6GUE protein in the case of the CDK2 enzyme ascribed to CRC, according to the PyMol software (Figure 10). The normal H-bonds were formed in part by the carboxyl and hydroxyl groups of the DCM ligand. At a greater binding affinity of −9.3 kcal/mol, Cu(II)–DCM interacted with the enzyme's Val-29 (through carboxylic C=O's oxygen), Glu-81 (by the coordinated H_2O hydrogen), Phe-82 and Lys-142 (through the oxygen of the coordinated H_2O), and Ser-247 (by the C–O carboxylate's oxygen) amino acids (Figure 10). In addition to its coordinated water molecules, the carboxylate COO^- group in the complex played a significant role in H-bonding with protein. Notably, the interaction between a series of imidazole-5-one compounds and the CDK2 enzyme (PDB ID: 6GUE) were reported, and the studied chemicals generated hydrogen bonds with the enzyme's amino acid residues with a binding affinity ranging from −10.8 to −11.0 kcal/mol [35]. Xiang et al. [64] described the molecular docking-based mechanism of glycitein in colon cancer treatment.

Table 4. Binding scores of DCM and Cu(II)-DCM with 6GUE (CRC) as a receptor protein.

Compound	Receptor	Binding Affinity(kcal/mol)	Interacting Amino Acids	Docking Parameters
L: 3,3′-dicarboxy-2,2′-dihydroxydiphenylmethane acid (DCM)	6GUE (implicated in the pathophysiology of CRC)	−7.2	Phe: 82; Glu: 81; His: 84; and Asn: 136	Exhaustiveness = 20; the center coordinates of the grid box are x = −29.066, y = −9.632, z = −0.1268; the dimensions of the grid box (Å) are x = 149.187, y = 124.808, and z = 142.086.
Complex: (Cu(II)–DCM)		−9.3	Val-29, Glu-81, Phe-82, Lys-142, and Ser-247	Exhaustiveness = 20; the center coordinates of the grid box are x = −26.0915, y = −6.129, and z = 20.136; the dimensions of the grid box (Å) are x = 126.936, y = 117.523, and z = 117.620.



DCM



Cu(II)–DCM

Figure 10. Interaction of DCM and its copper complex with 6GUE as a receptor.

3. Experimental Section

3.1. Materials and Procedures

The solvents and chemicals (salicylic acid, formaldehyde, sulfuric, copper (II) acetate monohydrate) used in this study were all BDH (Poole, UK) and used without any further purification. Sigma Company, located in St. Louis, MO, USA, supplied the trypan blue dye and MTT. Lonza (Verviers, Belgium) delivered the fetal bovine serum, DMEM, gentamycin, L-glutamine, HEPES buffer solution, and Trypsin-EDTA (0.25%). The American Type Culture Collection (ATCC, Rockville, MD, USA) supplied the human colon cancer cell line HCT–116. The Egypt Regional Center for Mycology and Biotechnology at Al-Azhar University (Cairo, Egypt) assessed the cytotoxicity. Table 5 depicts the other used procedures and techniques [37].

Table 5. Analyses and methodologies used for characterization.

Analysis	Appliance/Description
The melting point	The melting point in an open capillary tube was ascertained without correction using the George, Griffin melting point device.
C and H%	The elemental analysis for carbon and hydrogen was performed on Perkin Elmer 2400 at the Micro-Analytical Unit of Cairo University, Egypt.
Cu content	The Cu(II) content was determined by complexometric titration using EDTA in a hexamine buffer solution at pH = 6 [65].
IR spectra	The IR spectra were recorded using the ATR technique on Thermo Scientific's iS50 FT–IR spectrometer (Thermo Scientific company, Göteborg–Sweden) at Jouf University, KSA.
Electronic spectra	The Nujol mull method was used in the 200–1100 nm region using a Perkin–Elmer lambda 35 UV–Vis spectrophotometer (Perkin-Elmer company, Überlingen–Germany) at Al Azhar University, Egypt.
^{1}H-NMR	A Bruker spectrometer (400 MHz) was used in dimethylsulfoxide–d_6 at room temperature. Tetramethylsilane (TMS) was employed as the reference, and chemical shifts were provided in δ (ppm). The analysis was performed at the Regional Center of Mycology and Biotechnology, Cairo, Egypt.
Mass spectroscopy	The Thermo Scientific GCMS model ISQ was selected to confirm the molecular weight expectation using the direct inlet method.
Magnetic susceptibility	The magnetic susceptibility balance of the Johnson Metthy product (manufactured by Sherwood Scientific in Cambridge, UK) was used to determine the effective magnetic moment μ_{eff} at room temperature [66,67]. For this purpose, the relation applied to determine the mass magnetic susceptibility (χ_g) was as follows: $\chi_g = \frac{1.0034 \times (R - R_o) \times l}{(W_2 - W_1) \times 10^9}$ where R = the balance reading for the sample in the tube, R_o = the balance reading for the empty tube, l = the sample length in cm, W_2 = the weight of the sample and tube in gm, W_1 = the weight of the tube empty in gm, and χ_g = the mass magnetic susceptibility in c.g.s.
XRD	Using Germany's Bruker Co. D8 Discover XRD analyzer (Bruker company, Bremen, Germany), the crystallinity of DCM and the Cu(II)–DCM complex was examined at 3 to 80 degrees using Cu target K radiation (1.54 Å, 40 kV and 40 mA).
Morphology	A Quanta FEG 250 scanning electron microscope (FEI Company, Hillsboro, OR, USA) was used to obtain surface images of the copper complex where SEM stubs were used to mount the samples. For TEM investigation, a drop of solution was placed on the carbon-coated copper grids, and they were then left to dry out at room temperature by evaporation. A JEOL GEM–1010 transmission electron microscope was used to generate electron micrographs at 80 kV.

Table 5. *Cont.*

Analysis	Appliance/Description
Optical band gap, HOMO (Highest Occupied Molecular Orbital), and LUMO (Lowest Unoccupied Molecular Orbital) forms	The Tauc's equation, $\alpha h\upsilon = A(h\upsilon - E_g)^m$, was applied to estimate the energy gap (E_g) [68,69], where m is equal to 1/2 for direct transitions (electron–photon interacion) and 2 for indirect transitions (electron–photon–phonon interaction), respectively, and A is an energy-independent constant. The Chem. Draw Professional 16 program was used to identify the MM2 (molecular mechanics) and MMFF94 (molecular mechanics force field) energies, HOMO and LUMO forms, and optimal lowest energy structure for the compounds. The following particular Chem3D settings are utilized to minimize energy: (1) MM2 minimization (frame interval = 10, step interval = 2, target temperature = 300 K, minimum RMS gradient = 0.01) and (2) MMFF94 minimization (minimum RMS gradient = 0.100, maximum number of iterations = 500; Vander Vaals: cut off parameter = 10; electrostatic: dielectric exponent = 1, dielectric constant = 1).
DFT	DFT calculations were performed using the Gaussian 09 (G09) software package [70] by using the (B3LYP) level of theory [71]. A 6–31 g (d, p) basis set was used for C, H, and O atoms, and effective core potentials plus the Double Zeta (LanL2DZ) were employed for the Cu atom [72] for the present calculation. The ground-state geometric structure of the Cu(II)–DCM complex was fully optimized at the B3LYP level. Vibrational frequency calculations were conducted to confirm that the optimized geometry corresponds to a local minimum, indicated by exclusively positive eigenvalues. Vertical electronic excitations were then determined using TD-DFT (time-dependent density functional theory) [73] with the B3LYP functional in ethanol, modeled through CPCM [74].

3.2. Synthesis of Solid Compounds

3.2.1. DCM Ligand

For eight hours, a mixture of 27.6 g of salicylic acid, 180 g of sulfuric acid (50%), and 9.4 g of formaldehyde (30%) was refluxed on a hot plate. The separated powder was cooled, filtered out, and washed with cold water followed by a hot H_2O + EtOH mixture to remove any remaining unreacted salicylic acid. The compound was isolated and allowed to recrystallize from the acetone and exposed to air for 2 days. While insoluble in water, DCM is soluble in common organic solvents, e.g., acetone, diethyl ether, ethanol, carbon tetrachloride, dimethylformamide (DMF), and dimethylsulfoxide (DMSO). The structure of the isolated ligand was characterized by elemental analysis, IR, ^{1}H-NMR (Figure 11), and mass spectroscopy (Figure 12). Off-white powder, M.p. = 238 °C, yield 90%; found (%): H, 4.04; C, 62.60. $C_{15}H_{12}O_6$. Calculated (%): H, 4.20; C, 62.50. ^{1}H NMR, δ_{ppm}: 6.7–7.9 (aromatic protons, m, assigned as 7.49, 2H, d; 7.22–7.26, 2H, dd, and 6.78, 2H, d), 3.8 (CH_2, s), 11.6 (phenolic OH, s, broad), and 11.2 (COOH, s, broad). Water and DMSO (solvent) showed the chemical shift at around 3.8 and 2.5 ppm, respectively [75]. When D_2O was injected, the OH and COOH signals vanished, indicating that the groups were positioned correctly. Intermolecular hydrogen bonding between these groups was indicated by the broadening of the $OH_{phenolic}$ and COOH signals. *MS*, M^+: found (m/e): 288.35, $C_{15}H_{12}O_6$, = 288.35, as calculated. IR, Figure 13, (ATR, cm^{-1}): $\upsilon OH_{phenolic}$ (3150), $\upsilon C\text{-}O_{phenolic}$ (1281), $\delta OH_{phenolic}$ (1200), $\upsilon C\text{-}O_{carboxylic}$ (υ_{asym} = 1648 and υ_{sym} = 1372), aromatic C=C (1435, 1501, 1585, and 1609), 2905 (υCH_{asym}, methylene), 2836 (υCH_{sym}, methylene), 754 ($\delta CH_{rocking}$, methylene), 3033 ($\upsilon CH_{aromatic}$), and 791 ($\delta CH_{aromatic}$) [48]. In the solid state, DCM molecules exhibit intermolecular hydrogen bonding (O–H. . .O-H) because phenolic OH is detected at a lower frequency (3150 cm^{-1}) (Scheme 2). Due to internal conjugation, in which the carboxyl OH's lone pair resonates with C=O, and an infinite chain nature of DCM, the carboxyl group's υ (C=O) is lower than 1700–1730 cm^{-1} (usual range). UV-Vis spectroscopy (Nujol), λ_{max}

in nm: 280, 319, 341, 351, and 361 due to (π→π*, phenyl), (π→π*, phenolic OH), (π→π*, carboxylic C=O), (n→π*, phenolic OH), and (n→π*, carboxylic C=O), respectively.

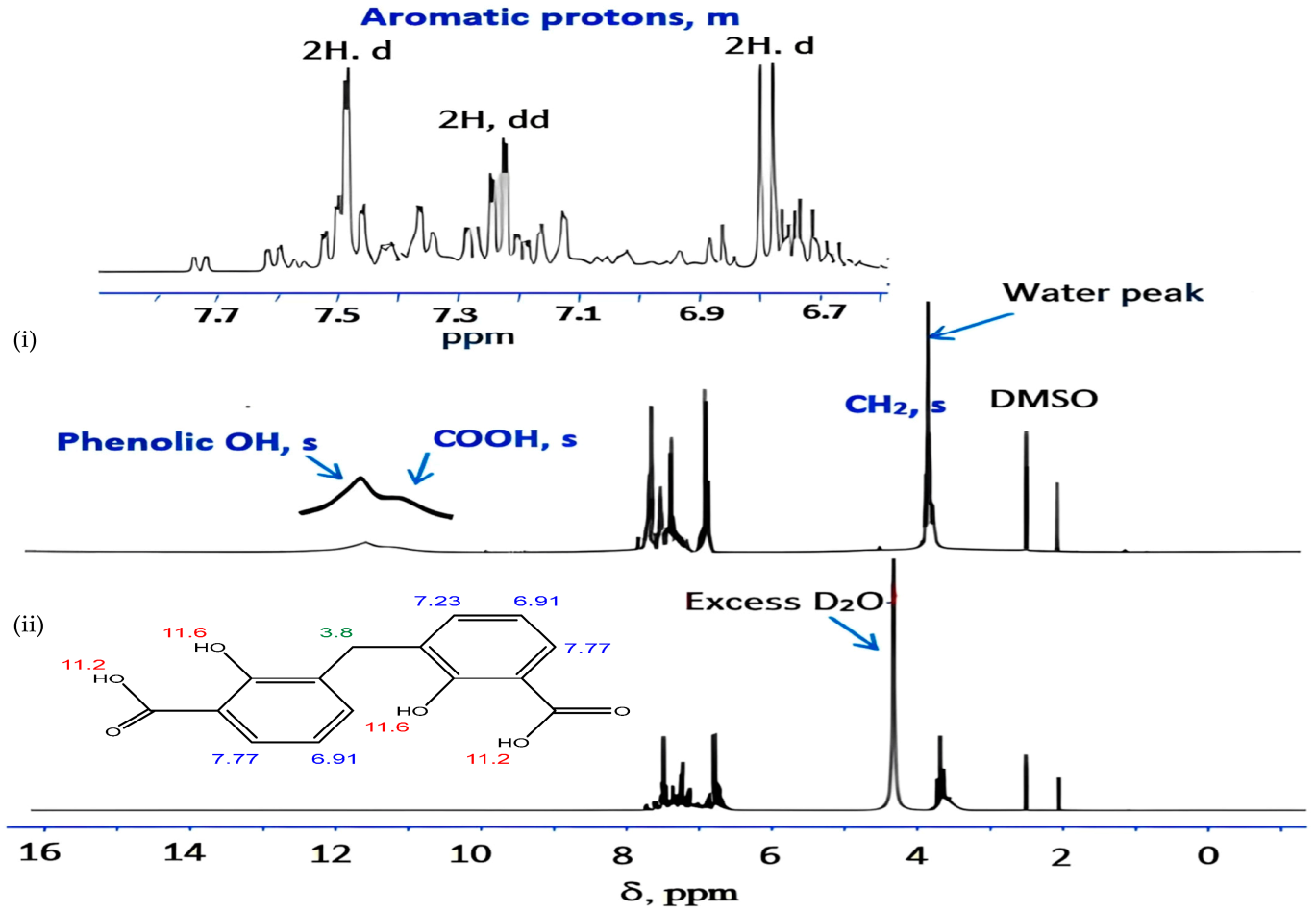


Figure 11. Proton NMR spectrum of DCM in (**i**) DMSO d_6 and (**ii**) DMSO d_6 + D_2O. Note: Numbers on the structure point to δ_{ppm} acquired by proton NMR analysis.

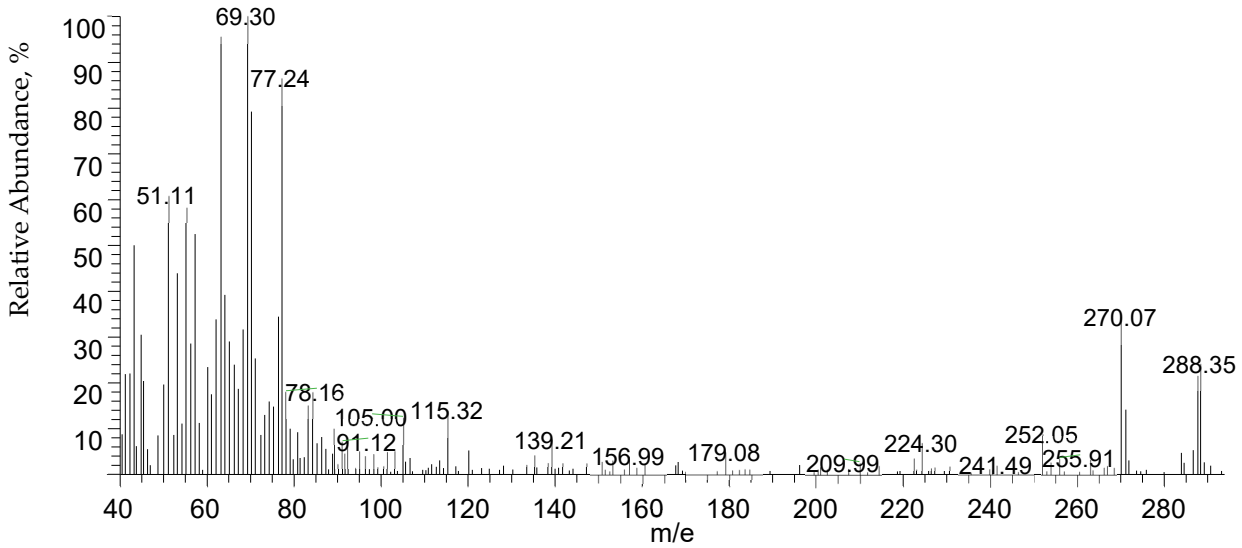


Figure 12. Mass spectrum of DCM.

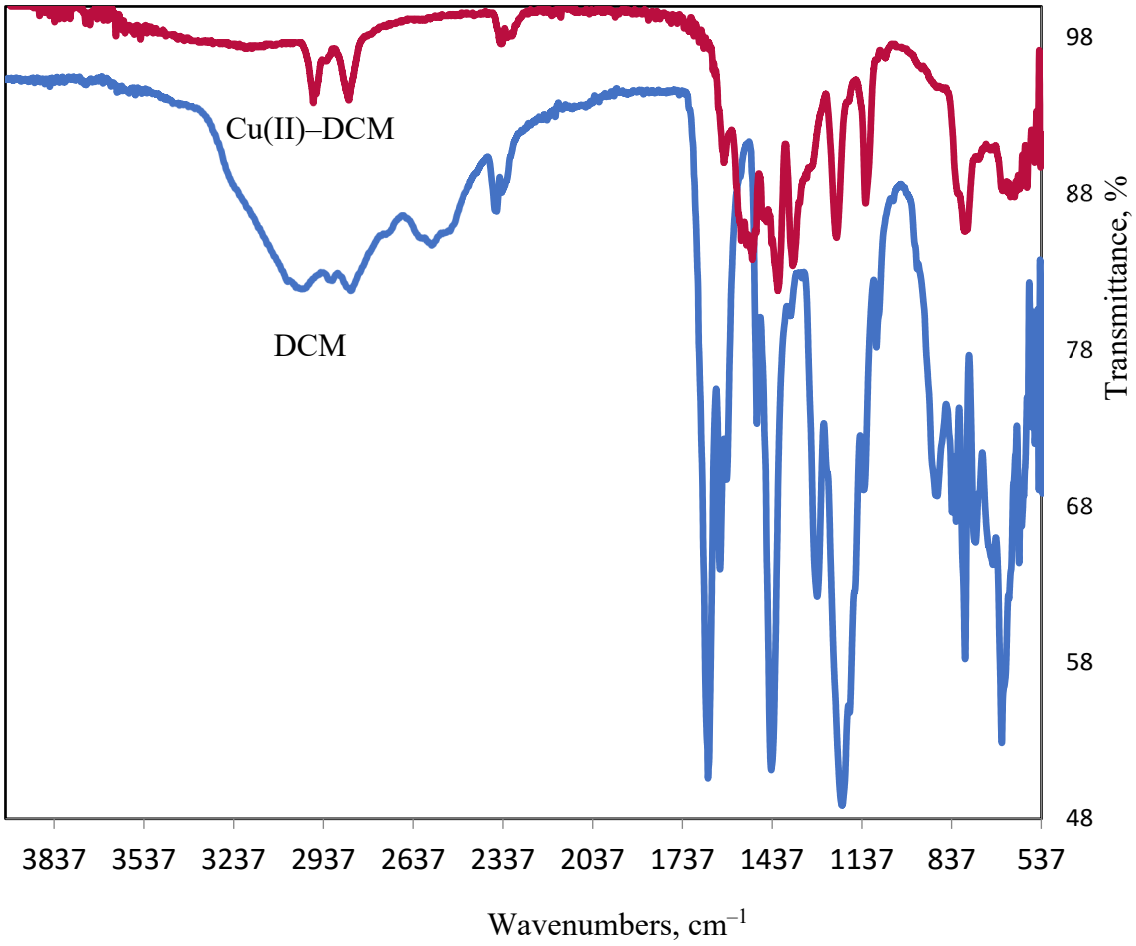
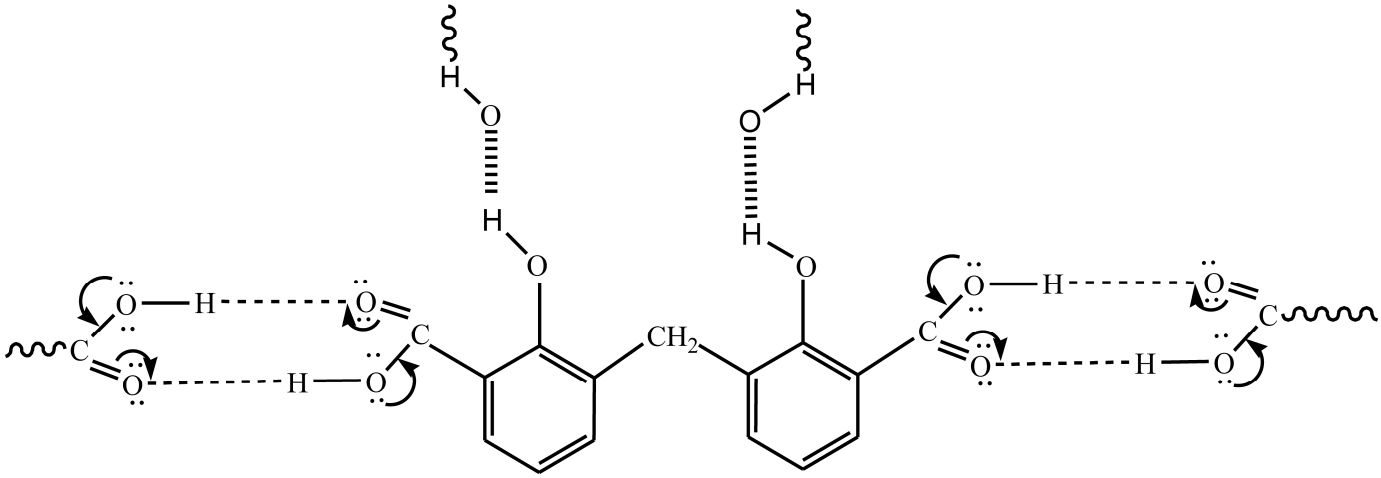


Figure 13. Ligand and copper complex FT-IR spectra.



Scheme 2. Infinite chain nature of DCM.

3.2.2. Cu(II)–DCM Complex

By adding ethanolic solution of 0.02 mole DCM to 0.04 mole Cu(II) acetate dissolved in ethanol, the Cu(II)–DCM complex was produced. The reaction mixture was refluxed on a water bath for four hours. The solid complex was filtered and carefully washed with hot EtOH prior to being air-dried. The complex is insoluble in water, alcohols, diethyl ether, carbon tetrachloride, acetone, DMF, and DMSO. The complex's insolubility nature in polar organic solvents suggests that the DCM ligand's polar groups (OH, COOH) have

disappeared as a result of its attachment to the Cu(II) ion. I.e., the hydroxyl and carboxyl groups were deprotonated. Brown powder, M.p. > 300 °C, yield 90%. Found (%): H, 3.46; C, 34.40; Cu, 24.76. $C_{15}H_{20}O_{12}Cu_2$. Calculated (%): H, 3.88; C, 34.69; Cu: 24.47.

3.3. Cytotoxicity Evaluation

To promote cell proliferation, 10% inactivated fetal calf serum and 104.7 µM of gentamycin were added to the RPMI 1640 medium. The cells were sub-cultured twice or three times a week and maintained at 37 °C in 5% CO_2 humidified atmosphere. In Corning 96-well tissue culture plates, tumor cell lines were suspended in media at a density of 5×10^4 cells/well for antitumor tests [76,77]. After that, the plates were incubated for an entire day. DMSO was used as solvent to solubilize the DCM ligand. The analyzed DCM was then added to 96-well plates in order to achieve 10 concentrations. For every concentration of the test sample, three wells were employed. Six vehicle controls with medium or DMSO (0.5%) were conducted as a control for each plate. The MTT test was used to calculate the number of viable cells following a 24 h incubation time. The plate's medium was quickly changed out for 100 µL of the brand-new, phenol red-free RPMI 1640 culture. Next, 10 µL of the 12 mM MTT stock solution (5 mg of MTT in 1 mL of PBS) was added to each well, including the untreated controls. The plates were then incubated at 37 °C with CO_2 (5%) for four hours. An 85 µL aliquot of the medium was removed from each well and then 50 µL of DMSO was added. The wells were then mixed using a pipette and the temperature was raised to 37 °C for 10 min. The number of viable cells was then computed as [(ODt/ODc)] × 100%. ODc is the mean optical density of untreated cells and ODt is the mean optical density of wells treated with the investigated compound. At 590 nm, the optical density was determined with the Sun Rise microplate reader manufactured by TECAN, Inc. Redwood City, CA 9406, in the USA. Plotting the concentration of residual cells and the compound produces the survival curve for the tumor cell line following DCM treatment. Using Graphpad Prism software, version 10 for Windows (San Diego, CA, USA), IC_{50} was calculated [78].

3.4. Molecular Docking (MD)

Molecular docking is a modeling method that determines the optimal binding pose between a ligand and a target's active site [79,80]. Using ChemDraw professional (v.16.0) software, the molecules' chemical structure was first precisely sketched. Next, energy reduction was carried out using Chem3D (v.16.0) and the MM2 tool. The PDB database (website: https://www.rcsb.org/ (accessed on 20 June 2024)) provided the protein 3D structures (ID: 6GUE). Using a PyRx-0.8 virtual screening program, molecular docking was carried out [81,82]. We generated a macromolecule or ligand by simply preparing the ligand and protein and (e.g., by removing water molecules, assigning partial charges, or adding hydrogen atoms) using the Autodock button of the PyRx software. Lastly, PyMol 2.5.8 (Python 3.9.18 64 bit) software was used to visualize the compound–protein binding mode [83]. Based on binding affinity (highest docking score), the optimal binding pose was identified.

4. Conclusions

One can create 3,3′-dicarboxy-2,2′-dihydroxydiphenylmethane (DCM) by combining formaldehyde, sulfuric acid, and salicylic acid. Different techniques can be used to describe DCM as well as its associated Cu(II) complex, namely elemental studies (C, H, M), FT–IR, MS, NMR, UV–Vis., PXRD, SEM, TEM, as well as magnetic measurements. The composition of the isolated Cu(II) complex is discovered to be in good accord with the proposed formulae when the elemental analysis percentages (H, C, and M%) from the

theoretical and experimental analyses are compared. The square-planar configuration of the Cu(II)–3,3′-dicarboxy-2,2′-dihydroxydiphenylmethane complex (Cu(II)–DCM) was the conclusion. The Cu(II)–DCM complex's amorphous nature makes it suitable for application in the production of flexible and bending electronics. Additionally, it can be utilized to produce medications with enhanced bioavailability and resistant coatings. The optical energy gap of the free DCM is reduced when it coordinates with Cu(II) ions. It has been found that the refractive index values vary upon chelation. The specimen's optical conductivity changes or rises in response to changes in photon energy or frequency. Up to 3.5 eV, light penetrates the ligand with greater ease than the complex, and the penetration depth varies with the photon energy. These optical characteristics could be useful in a variety of fields, including semiconductors and electronic devices. The Cu(II)–DCM complex demonstrates stable coordination with significant electronic interactions between the Cu(II) ion and DCM ligand, as shown by the optimized structural parameters and NBO analysis. The decrease in the energy gap from the ligand to the complex indicates enhanced electronic reactivity and potential for charge transfer. the TD-DFT calculations in ethanol closely match the experimental absorption maximum, confirming the model's reliability in simulating electronic transitions within polar environments. DCM was tested on human colon (HCT–116) cancer cells, and the inhibitory impact was evaluated. Based on the experiment results, DCM gave a respectable effect to prevent 50% of cell multiplication for colon cancer. Since the structure of DCM is comparable to that of a naturally occurring, non-toxic salicylic acid, this result might be welcomed. According to the virtual screening (molecular docking study), future medications for the treatment of colorectal cancer may be developed utilizing the compounds under investigation, which are potent inhibitors of the target proteins, particularly the copper complex. Despite the insolubility of the Cu(II) complex, its improved binding affinity (−9.3 kcal/mol) qualifies it to be used in the field of treatment. It may enter the body through ingestion, inhalation, etc. However, a lot of research in the field of biology can be conducted to further clarify the biological activity showing possibility of use on humans.

Author Contributions: Conceptualization, A.H.A., K.A.S. and I.O.A.; Methodology, I.O.A., K.A.S., S.A. and E.K.A.; software, A.H.A., K.A.S., S.A. and E.K.A.; Validation, A.H.A., Y.M.A., S.A., K.A.S. and E.K.A.; Formal analysis, A.H.A., K.A.S., E.S.G., I.O.A., Y.M.A., S.A. and E.K.A.; Investigation, A.H.A., E.S.G., K.A.S. and S.A.; Data curation, K.A.S., Y.M.A. and E.K.A.; Writing—original draft, A.H.A. and K.A.S.; Writing—review & editing, A.H.A., I.O.A., K.A.S., Y.M.A., E.S.G., S.A. and E.K.A.; Visualization, A.H.A. and K.A.S.; Project administration, A.H.A.; Funding acquisition, A.H.A., S.A. and E.K.A. All authors have read and agreed to the published version of the manuscript.

Funding: This work was funded by the Deanship of Graduate Studies and Scientific Research at Jouf University under grant no. (DGSSR-2023-02-02100).

Institutional Review Board Statement: Not applicable.

Informed Consent Statement: Not applicable.

Data Availability Statement: Data are contained within the article.

Conflicts of Interest: The authors declare no conflicts of interest.

References

1. Parulerkar, M.H.; Bhatt, H.A.; Potnis, S.P. New Intermediates for Plastics and Coatings: 1. Preparation and Characterization of Methylene-di-salicylic-acid. *J. Ind. Chem. Soc.* **1972**, *49*, 1201–1207.
2. Gao, F.; Chunji, N.; Jiazuan, N. Study on Mixed Ligand Complexes of Rare Earth with Nitrilotriacetic Acid and Amino acid. *Chin. J. Appl. Chem.* **1990**, *3*, 10–13. [CrossRef]
3. Trevin, S.; Bedioui, F.; Gomez, M.G.; Charreton, C.B. Electro Polymerized Nickel Micro Cyclic Complex–Base Films Design and Elctro–catalytic Application. *J. Mater. Chem.* **1997**, *7*, 923–928. [CrossRef]

4. Ahmed, A.H.; Sherif, E.M. Methylenedisalicylic Acid as a Bio Corrosion Inhibitor for Aluminum in Concentrated Sodium Chloride Solutions. *ACS Omega* **2022**, *7*, 19193–19203. [CrossRef]
5. Ahmed, A.H.; Althobaiti, I.O.; Aljohani, M.; Gad, E.S.; Asiri, Y.M.; Hussein, O.A. Mammalian Cell Cytotoxicity, Antibacterial Activity and the Properties of Methylenebis(hydroxybenzoic acid) and Its Related Zinc(II) Complex. *Crystals* **2024**, *14*, 88. [CrossRef]
6. Ahmed, A.H.; Althobaiti, I.O.; Alenezy, E.K.; Asiri, Y.M.; Ghalab, S.; Hussein, O.A. Characterization and Cytotoxic Assessment of Bis(2-hydroxy-3-carboxyphenyl)methane and Its Nickel(II) Complex. *Molecules* **2024**, *29*, 4239. [CrossRef]
7. Clemmensen, E.; Heitman, A.H.C. Methylenedisalicylic Acid and Its Reaction with Bromine and Iodine. *J. Am. Chem. Soc.* **1911**, *33*, 733–745. [CrossRef]
8. Sivapullaiah, P.V.; Soundararajan, S. Methylene di Salicylates of Rare–Earths. *J. Indian Inst. Sci.* **1976**, *58*, 289–293.
9. Tobita, S.; Arakawa, M.; Tanaka, I. The Paramagnetic Metal Effect on the Ligand Localized S1. apprx. fwdarw. T1 Intersystem Crossing in the Rare–Earth–Metal Complexes with Methyl Salicylate. *J. Phys. Chem.* **1985**, *89*, 5649–5654. [CrossRef]
10. Patel, R.P.; Karampurwala, A.M.; Shah, J.R. Physicochemical Studies on Square Planar Co^{2+}, Ni^{2+} and Cu^{2+} Chelate Polymers. *Macromol. Mater. Eng.* **1980**, *87*, 87–94.
11. Han, Z.X.; Wang, J.J.; Hu, H.M.; Chen, X.L.; Wu, Q.R.; Li, D.S.; Shi, Q.Z. Effects of the Size of Aromatic Chelate Ligands and d^{10} Metal Ions on the Structures of Dicarboxylate Complexes: From Dinuclear Molecule to Helical Chains and 2D Network. *J. Mol. Struct.* **2008**, *891*, 364–369. [CrossRef]
12. Shi, X.M.; Li, M.X.; He, X.; Liu, H.-J.; Shao, M. Crystal Structures and Properties of Four Coordination Polymers Constructed from Flexible Pamoic Acid. *Polyhedron* **2010**, *29*, 2075–2080. [CrossRef]
13. Zhang, L.N.; Sun, X.L.; Du, C.X.; Hou, H.W. Structural Diversity and Fluorescent Properties of New Metal–Organic Frameworks Constructed from Pamoic Acid and Different N-Donor Ligands. *Polyhedron* **2014**, *72*, 90–95. [CrossRef]
14. Tang, Y.Z.; Xiong, J.B.; Tan, Y.H.; Wang, Y.; Deng, Y.P.; Xu, Q.; Wen, H.R. Solvothermal Syntheses, Crystal Structures and Photoluminescent Properties of Four Coordination Polymers with Pamoic Acid and Pyridine mixed Ligands. *Inorganica Chim. Acta* **2014**, *410*, 82–87. [CrossRef]
15. Kerraj, S.; Salah, M.; Chtita, S.; El Idrissi, M.; Belaaouad, S.; Mohammed, M.; Acharjee, N.; Komiha, N. Theoretical Study of Photovoltaic Performances of Ru, Rh and Ir Half Sandwich Complexes Containing N,N Chelating Ligands in Dye-Sensitized Solar Cells (DSSCs). DFT and TD-DFT Investigation. *Comput. Theor. Chem.* **2022**, *1209*, 113630. [CrossRef]
16. Kherrouba, A.; Bensegueni, R.; Guergouri, M.; Boulkedid, A.-L.; Boutebdja, M.; Bencharif, M. Synthesis, cCystal Structures, Optical Properties, DFT and TD-DFT Studies of Ni (II) Complexes with Imine-Based ligands. *J. Mol. Struct.* **2022**, *1247*, 131351. [CrossRef]
17. Patra, A.; Puschmann, H.; Manna, S.C. Bidentate Schiff Base Coordinated Square Planer Nickel(II) Complexes: Synthesis, Crystal Structure, DFT/TD-DFT Calculation and DNA/Protein binding. *Polyhedron* **2021**, *201*, 115146. [CrossRef]
18. Jouypazadeh, H.; Farrokhpour, H.; Karbasizadeh, M.; Hadadzadeh, H. Water-Vapochromic Behavior of a Mononuclear Pd(II) Complex of Piroxicam: A DFT and TD-DFT study. *J. Mol. Graph. Model.* **2021**, *102*, 107773. [CrossRef]
19. Brahim, H. DFT/TD-DFT Investigation on the UV–vis Absorption and Phosphorescence Spectra of Platinum(II) and Palladium(II) Complexes with Schiff-Base Ligands. *J. Lumin.* **2019**, *210*, 96–103. [CrossRef]
20. Luňák, S.; Aysha, T.; Lyčka, A.; Machalický, O.; Hrdina, R. Structure and Absorption of Co(III) Azo Complex Dyes Based on Pyrrolinone esters: DFT and TD DFT Study. *Chem. Phys. Lett.* **2014**, *608*, 213–218. [CrossRef]
21. Aglan, H.A.; Ahmed, H.H.; El-Toumy, S.A.; Mahmoud, N.S. Gallic Acid Against Hepatocellular Carcinoma: An Integrated Scheme of the Potential Mechanisms of Action from In Vivo Study. *Tumor Biol.* **2017**, *39*, 1010428317699127. [CrossRef] [PubMed]
22. Simon, L.; Imane, A.; Srinivasan, K.K.; Pathak, L.; Daoud, I. In Silico Drug-Designing Studies on Flavanoids as Anticolon Cancer Agents: Pharmacophore Mapping, Molecular Docking, and Monte Carlo Method-Based QSAR Modeling. *Interdiscip. Sci.* **2017**, *9*, 445–458. [CrossRef] [PubMed]
23. Swetha, M.; Keerthana, C.; Rayginia, T.P.; Anto, R.J. Cancer Chemoprevention: A Strategic Approach Using Phytochemicals. *Front. Pharmacol.* **2021**, *12*, 809308.
24. Selvam, C.; Prabu, S.L.; Jordan, B.C.; Purushothaman, Y.; Umamaheswari, A.; Zare, M.S.H.; Thilagavathi, R. Molecular Mechanisms of Curcumin and Its Analogs in Colon Cancer Prevention and Treatment. *Life Sci.* **2019**, *239*, 117032. [CrossRef]
25. Lin, M.H.; Cheng, C.H.; Chen, K.C.; Leem, W.T.; Wang, Y.F.; Xiao, C.Q.; Lin, C.W. Induction of ROS–Independent JNK–Activation–Mediated Apoptosis by a Novel Coumarin–Derivative, DMAC, in Human Colon Cancer Cells. *Chem. Biol. Interact.* **2014**, *218*, 42–49. [CrossRef]
26. Qian, Y.; Shi, C.; Cheng, C.; Liao, D.; Liu, J.; Chen, G. Ginger Polysaccharide UGP1 Suppressed Human Colon Cancer Growth Via p53, Bax/Bcl–2, Caspase–3 Pathways and Immunomodulation. *Food Sci. Hum. Wellness* **2023**, *12*, 467–476. [CrossRef]
27. De, S.; Paul, S.; Manna, A.; Majumder, C.; Pal, K.; Casarcia, N.; Mondal, A.; Banerjee, S.; Nelson, V.K.; Ghosh, S.; et al. Phenolic Phytochemicals for Prevention and Treatment of Colorectal Cancer: A Critical Evaluation of In Vivo Studies. *Cancers* **2023**, *15*, 993. [CrossRef]

28. Ghasemzadeh, A.; Jaafar, H.; Karimi, E.; Ghasemzadeh, A.; Jaafar, H.Z.E.; Karimi, E. Involvement of Salicylic Acid on AntiOxidant and Anticancer Properties, Anthocyanin Production Anthocyanin Production and Chalcone Synthase Activity in Ginger (*Zingiber officinale* Roscoe) Varieties. *Int. J. Mol. Sci.* **2012**, *13*, 14828–14844. [CrossRef]
29. Kalinowska, M.; Mazur, L.; Jabłońska–Trypuć, A.; Lewandowski, W. A New Calcium 2,5–dihydroxybenzoate: Synthesis, Characterization and Antioxidant Studies and Stress Mediated Cytotoxity in MCF-7 cells. *J. Saud. Chem. Soc.* **2018**, *22*, 742–756. [CrossRef]
30. Bonta, R.K. Dietary Phenolic Acids and Flavonoids as Potential Anti–Cancer Agents: Current State of the Art and Future Perspectives, Anti-Cancer Agent. *Anti-Cancer Agents Med. Chem.* **2020**, *20*, 29–48. [CrossRef]
31. Kattan, S.W.; Nafie, M.S.; Elmgeed, G.A.; Alelwani, W.; Badar, M.; Tantawy, M.A. Molecular Docking, Anti-Proliferative Activity and Induction of Apoptosis in Human Liver Cancer Cells Treated with Androstane Derivatives: Implication of PI3K/AKT/mTOR Pathway. *J. Steroid. Biochem. Mol. Biol.* **2020**, *198*, 105604. [CrossRef] [PubMed]
32. Meng, X.; Zhang, H.; Mezei, M.; Cui, M. Molecular Docking: A Powerful Approach for Structure-Based Drug Discovery. *Curr. Comput. Aided Drug. Des.* **2011**, *7*, 146–157. [CrossRef] [PubMed]
33. Clarke, J.M.; Hurwitz, H.I. Targeted Inhibition of VEGF Receptor 2: An Update on Ramucirumab. *Expert. Opin. Biol. Ther.* **2013**, *13*, 1187–1196. [CrossRef]
34. Kolligs, F.T. Diagnostics and Epidemiology of Colorectal Cancer. *Visc. Med.* **2016**, *32*, 158–164. [CrossRef]
35. Ikwu, F.A.; Isyaku, Y.; Obadawo, B.S.; Lawal, H.A.; Ajibowu, S.A. In Silico Design and Molecular Docking Study of CDK2 Inhibitors with Potent Cytotoxic Activity Against HCT116 Colorectal Cancer Cell Line. *J. Genet. Eng. Biotechnol.* **2020**, *18*, 51. [CrossRef]
36. Ejidike, I.P.; Bamigboye, M.O.; Clayton, H.S. Spectral, In Vitro Antiradical and Antimicrobial Assessment of Copper Complexes Containing Tridentate Schiff Base Derived from Dihydroxybenzene Functionality with Diaminoethylene Bridge. *Spectrosc. Lett.* **2021**, *54*, 212–230. [CrossRef]
37. Thabet, M.S.; Ahmed, A.H. Ship–in–a–Bottle Synthesis and Physicochemical Studies on Zeolite Encapsulated Mn(II), Mn(III)–Semicarbazone Complexes: Application in the Heterogeneous hydroxylation of Benzene. *J. Porous Mater.* **2013**, *20*, 319–330. [CrossRef]
38. Lal, R.A.; Basumatary, D.; Arjun, K.D.; Kumar, A. Synthesis and Spectral Characterization of Copper(II), Nickel(II) and Manganese(II) Complexes Derived from Bis(2–hydroxy–1–naphthaldehyde) Malonoyldihydrazone. *Transit. Met. Chem.* **2007**, *32*, 481–493. [CrossRef]
39. Choroba, K.; Machura, B.; Szlapa-Kula, A.; Malecki, J.G.; Raposo, L.; Roma-Rodrigues, C.; Cordeiro, S.; Baptista, P.V.; Fernandes, A.R. Square Slanar Au(III), Pt(II) and Cu(II) Complexes with Quinoline-Substituted 2,2′:6′,2″-terpyridine Ligands: From In Vitro to In Vivo Biological Properties. *Eur. J. Med. Chem.* **2021**, *218*, 113404. [CrossRef]
40. Ahmed, A.H.; Moustafa, M.G. Spectroscopic, Morphology and Electrical Conductivity Studies on Co(II), Ni(II), Cu(II) and Mn(II)–oxaloyldihydrazone complexes. *J. Saudi Chem. Soc.* **2020**, *24*, 381–392. [CrossRef]
41. Du, M.; Li, C.P.; Zhao, X.J.; Yu, Q. Interplay of Coordinative and Supramolecular Interactions in Engineering Unusual Crystalline Architectures of Low-Dimensional Metal–Pamoate Complexes under Co-Ligand Intervention. *Cryst. Eng. Comm.* **2007**, *9*, 1011–1028. [CrossRef]
42. Joseyphus, R.S.; Nair, M.S. Synthesis, Characterization and Biological Studies of Some Co(II), Ni(II) and Cu(II) Complexes Derived from Indole–3–carboxaldehyde and Glycylglycine, as Schiff Base Ligand. *Arab. J. Chem.* **2010**, *3*, 195–204. [CrossRef]
43. Liu, B.; Zhang, Y.-J.; Yang, B. Two novel Cr(III) Complexes $[Cr(SA)_2(en)]$TBA and $[Cr(SA)(en)_2]$Br: Synthesis, Characterization and Spectral Studies. *Inorg. Chem. Commun.* **2013**, *30*, 163–167. [CrossRef]
44. Hayashita, T.; Higuchi, T.; Sawano, H.; Marchand, A.P.; Kumar, K.A.; Bott, S.G.; Mlinarić-Majerski, K.; Sumanovac, T.; Elkarim, N.S.; Hwang, H.S.; et al. Molecular Design of Lipophilic Disalicylic Acid Compounds with Varying Spacers for Selective Lead(II) extraction. *Talanta* **2000**, *30*, 385–396. [CrossRef]
45. Patterson, A. The Scherrer Formula for X-Ray Particle Size Determination. *Phys. Rev.* **1939**, *56*, 978–982. [CrossRef]
46. Streetman, B.G. *Solid State Electronic Devices*, 5th ed.; Prentice: Hoboken, NJ, USA, 2000.
47. Elliott, R.J. Symmetry of Excitons in Cu_2O. *Phys. Rev.* **1961**, *124*, 340. [CrossRef]
48. Sengupta, S.K.; Pandey, O.P.; Srivastava, B.K.; Sharma, V. Trends in Structural Mechanics: Theory, Practice. *Transit. Met. Chem.* **1998**, *23*, 349–353. [CrossRef]
49. Turan, N.; Gündüz, B.; Körkoca, H.; Adigüzel, R.; Çolak, N.; Buldurun, K. Study of Structure and Spectral Characteristics of the Copper(II) and Copper(II) Complexes with 5,5–dimethyl–2–(2–(3–nitrophenyl)hydrazono)cyclohexane–1,3–dione and Their Effects on Optical Properties and the Developing of the Energy Band Gap and Investigation of Antibacterial Activity. *J. Mex. Chem. Soc.* **2014**, *58*, 65–75.
50. Gittleman, J.I.; Sichel, E.K.; Arie, Y. Composite Semiconductors: Selective Absorbers of Solar Energy. *Sol. Energy Mater.* **1979**, *1*, 93–104. [CrossRef]

51. Belmokhtar, A.; Yahiaoui, A.; Hachemaoui, A.I.; Abdelghani, B.; Sahli, N.; Belbachir, M. A Novel Poly{(2,5–diylfuran)(benzylidene)}: A New Synthetic Approach and Electronic Properties. *ISRN Phys. Chem.* **2012**, *2012*, 781879. [CrossRef]
52. Yakuphanoglu, F.; Erten, H. Refractive Index Dispersion and Analysis of the Optical Constants of an Ionomer Thin Film. *Opt. Appl.* **2005**, *4*, 969–976.
53. Paul, T.C.; Podder, J. Synthesis and Characterization of Zn–incorporated TiO_2 Thin Films: Impact of Crystallite Size on X-Ray Line Broadening and Bandgap Tuning. *Appl. Phys. A* **2019**, *125*, 818. [CrossRef]
54. Calderón-Jiménez, B.; Montoro-Bustos, A.R.; Pereira-Reyes, R.; Paniagua, S.A.; Vega-Baudrit, J.R. Novel Pathway for the Sonochemical Synthesis of Silver Nanoparticles with Near-Spherical Shape and High Stability in Aqueous Media. *Sci. Rep.* **2022**, *12*, 882. [CrossRef]
55. Min, H.S. The Influence of Concentration on the Formation of Chemical Bath Deposited Copper Tin Sulphide Thin Films: SEM and EDX Studies. *J. Chem. Eng. Res. Updates* **2022**, *9*, 22–29.
56. Ejidike, I.P.; Direm, A.; Parlak, C.; Adeniyi, A.A.; Ata, M.A.; Eze, M.O.; Hollett, J.W.; Clayton, H.S. Spectroscopic Characterization, DFT Calculations, in Vitro Pharmacological Potentials, and Molecular Docking Studies of *N*,*N*,*O*-Schiff Base and Its Trivalent Metal Complexes. *Chem. Phys. Impact* **2024**, *8*, 100549. [CrossRef]
57. Tabares-Mendoza, C.; Guadarrama, P. Predicting the Catalytic Efficiency by Quantum-Chemical Descriptors: Theoretical Study of Pincer Metallic Complexes Involved in the Catalytic Heck Reaction. *J. Organomet. Chem.* **2006**, *691*, 2978–2986. [CrossRef]
58. Saren, D.; Das, S.; Paul, A.; Tat, S.S.; Santra, M.K.; Si, T.K.; Puschmann, H.; Manna, S.C. Tris Chelated Meridional Isomers of Co(III) Complexes: Synthesis, Crystal Structure, Protein Binding, Cytotoxicity Studies and DFT/TDDFT Calculation. *Inorg. Chim. Acta* **2023**, *550*, 121423. [CrossRef]
59. Kargar, H.; Fallah-Mehrjardi, M.; Behjatmanesh-Ardakani, R.; Bahadori, M.; Moghadam, M.; Ashfaq, M.; Munawar, K.S.; Tahir, M.N. Pd(II) and Ni(II) Complexes Containing ONNO Tetradentate Schiff Base Ligand: Synthesis, Crystal Structure, Spectral Characterization, Theoretical Studies, and Use of PdL as an Efficient Homogeneous Catalyst for Suzuki–Miyaura Cross-Coupling Reaction. *Polyhedron* **2022**, *213*, 115622. [CrossRef]
60. Ahmed, A.H. N,N′–Bis[2–hydroxynaphthylidene]/[2–methoxybenzylidene]amino]oxamides and Their Divalent Manganese Complexes: Isolation, Spectral Characterization, Morphology, Antibacterial and Cytotoxicity Against Leukemia Cells. *Open Chem.* **2020**, *18*, 426–437. [CrossRef]
61. Varga, I.; Luburić, D.B.; Kolanovic, B.S.; Varenina, I.K.; Bilandžić, N. Salicylic Acid-a Medicine with Various Healing Properties. *Vet. Stanica* **2018**, *49*, 413–422.
62. Wiśniewska, J.; Klasik-Ciszewska, S.; Duda-Grychtoł, K. Salicylic Acid and Its Use in Cosmetology. *Aesth. Cosmetol. Med.* **2023**, *12*, 91–95. [CrossRef]
63. Jain, A.N. Surflex: Fully Automatic Flexible Molecular Docking Using a Molecular Similarity-Based Search Engine. *J. Med. Chem.* **2003**, *46*, 499–511. [CrossRef] [PubMed]
64. Xiang, T.; Jin, W. Mechanism of Glycitein in the Treatment of Colon Cancer Based on Network Pharmacology and Molecular Docking. *Lifestyle Genom.* **2023**, *16*, 1–10. [CrossRef]
65. Vogel, A.I. *A Text Book of Quantitative Inorganic Analysis*; Longmans: London, UK, 1961.
66. Ahmed, A.H.; Thabet, M.S. Metallo–Hydrazone Complexes Immobilized in ZeoliteY: Synthesis, Identification and Acidviolet–1 Degradation. *J. Mol. Struct.* **2011**, *1006*, 527–535. [CrossRef]
67. Drago, R.S. *Physical Methods in Inorganic Chemistry*, 1st ed.; Affiliated East–West Press Pvt. Ltd.: Darya Ganj, New Delhi, India, 2012.
68. Mott, N.F.; Davis, E.A. *Electronic Processes in Non–Crystalline Materials*, 2nd ed.; Clarendon Press: Oxford, UK, 1979.
69. Ahmed, A.H.; Hassan, A.M.; Gumaa, H.A.; Mohamed, B.H.; Eraky, A.M.; Omran, A.A. Copper(II)–Oxaloyldihydrazone Complexes: Physico–Chemical Studies; Energy Band Gap and Inhibition Evaluation of Free Oxaloyldihydrazones Toward the Corrosion of Copper metal in Acidic Medium. *Arab. J. Chem.* **2019**, *12*, 4287–4302. [CrossRef]
70. Frisch, M.J.; Trucks, G.W.; Schlegel, H.B.; Scuseria, G.E.; Robb, M.A.; Cheeseman, J.R.; Scalmani, G.; Barone, V.; Mennucci, B.; Petersson, G.A.; et al. *Gaussian 09, Rev. D.01*; Gaussian Inc.: Wallingford, CT, USA, 2009.
71. Lee, C.; Yang, W.; Parr, R.G. Development of the Colle-Salvetti Correlation-Energy Formula into a Functional of the Electron Density. *Phys. Rev. B* **1988**, *37*, 785–789. [CrossRef]
72. Hay, P.J.; Wadt, W.R. Ab Initio Effective Core Potentials for Molecular Calculations. Potentials for the Transition Metal Atoms Sc to Hg. *J. Chem. Phys.* **1985**, *82*, 270–283. [CrossRef]
73. Cossi, M.; Barone, V. Time-Dependent Density Functional Theory for Molecules in Liquid Solutions. *J. Chem. Phys.* **2001**, *115*, 4708–4717. [CrossRef]
74. Cossi, M.; Rega, N.; Scalmani, G.; Barone, V. Energies, Structures, and Electronic Properties of Molecules in Solution with the C-PCM Solvation model. *J. Comput. Chem.* **2003**, *24*, 669–681. [CrossRef]

75. Haque, R.A.; Iqbal, M.A.; Khadeer, M.B. Design, Synthesis and Structural Studies of Meta-Xylyl Linked Bis-Benzimidazolium Salts: Potential Anticancer Agents Against Human Colon Cancer. *Chem. Cent. J.* **2012**, *6*, 68. [CrossRef]
76. Abo-Ashour, M.F.; Eldehna, W.M.; Nocentini, A.; Bonardi, A.; Bua, S.; Ibrahim, H.S.; Elaasser, M.M.; Kryštof, V.; Jorda, R.; Gratteri, P. 3-Hydrazinoisatin-Based Benzenesulfonamides as Novel Carbonic Anhydrase Inhibitors Endowed with Anticancer Activity: Synthesis, in Vitro Biological Evaluation and in Silico Insights. *Eur. J. Med. Chem.* **2019**, *184*, 111768. [CrossRef] [PubMed]
77. Gomha, S.M.; Riyadh, S.M.; Mahmmoud, E.A.; Elaasser, M.M. Synthesis and Anticancer Activities of Thiazoles, 1,3-Thiazines, and Thiazolidine Using Chitosan-rafted-poly(vinylpyridine) as Basic Catalyst. *Heterocycles* **2015**, *91*, 1227–1243.
78. Mosmann, T. Rapid Colorimetric Assay for Cellular Growth and Survival: Application to Proliferation and Cytotoxicity Assays. *J. Immunol. Methods* **1983**, *65*, 55–63. [CrossRef]
79. Albqmi, M.; Elkanzi, N.A.A.; Ali, A.M.; Abdou, A. Design, Characterization, and DFT Exploration of New Mononuclear Fe(III) and Co(II) Complexes Based on Isatin-hydrazone Derivative: Anti-Inflammatory Profiling and Molecular Docking Insights. *J. Mol. Struct.* **2025**, *1319*, 139494. [CrossRef]
80. Mert, S.; Demir, Y.; Sert, Y.; Kasımoğulları, R.; Gülçin, İ. Synthesis, Biological Evaluation and Molecular Docking of Novel Pyrazole Derivatives as Multitarget Acetylcholinesterase and Carbonic Anhydrase Inhibitors. *J. Mol. Struct.* **2025**, *1319*, 139472. [CrossRef]
81. Mustafa, G.; Younas, S.; Mahrosh, H.S.; Albeshr, M.F.; Bhat, E.A. Molecular Docking and Simulation-Binding Analysis of Plant Phytochemicals with the Hepatocellular Carcinoma Targets Epidermal Growth Factor Receptor and Caspase-9. *Molecules* **2023**, *28*, 3583. [CrossRef]
82. Coumar, M.S. *Molecular Docking for Computer-Aided Drug Design: Fundamentals, Techniques, Resources and Applications*, 1st ed.; Academic Press: Cambridge, MA, USA, 2021.
83. Zhang, Y.; Zhao, Z.; Li, W.; Tang, Y.; Wang, S. Mechanism of Taxanes in the Treatment of Lung Cancer Based on Network Pharmacology and Molecular Docking. *Curr. Issues Mol. Biol.* **2023**, *45*, 6564–6582. [CrossRef]

Disclaimer/Publisher's Note: The statements, opinions and data contained in all publications are solely those of the individual author(s) and contributor(s) and not of MDPI and/or the editor(s). MDPI and/or the editor(s) disclaim responsibility for any injury to people or property resulting from any ideas, methods, instructions or products referred to in the content.